Icarus 302 (2018) 343–359

Contents lists available at ScienceDirect

Icarus

journal homepage: www.elsevier.com/locate/icarus

Internal structure of asteroid gravitational aggregates

Adriano Campo Bagatin [a,b,*], Rafael A. Alemañ [a,b], Paula G. Benavidez [a,b], Derek C. Richardson [c]

[a] Departamento de Física, Ingeniería de Sistema y Teoría de la Señal, Escuela Politécnica Superior, Universidad de Alicante, P.O. Box 99, Alicante, 03080 Spain
[b] Instituto de Física Aplicada a las Ciencias y la Tecnología, Universidad de Alicante, P.O. Box 99, Alicante, 03080 Spain
[c] Department of Astronomy, University of Maryland, College Park, MD 20742, USA

ARTICLE INFO

Article history:
Received 2 August 2017
Revised 9 November 2017
Accepted 20 November 2017
Available online 22 November 2017

Keywords:
Asteroids
Interiors
Collisional physics

ABSTRACT

The internal structure of small asteroids is fundamentally unknown due to lack of direct measurements. The only clues on this topic come from theoretical considerations and from the comparison between measured bulk densities of asteroids and their corresponding analogue meteorite densities. The mass distribution and the void space between components in a gravitational aggregate determine the structure of such objects. In this paper we study numerically the dynamical and collisional evolution of the reaccumulation process of the fragments created in catastrophic collisions of asteroids in the 500 m to 10 km size range. An effort to consider irregularly shaped fragments is made by taking advantage of the results of laboratory experiments that provide relative mass distributions and aspect ratios for fragment shapes. We find that the processes that govern the final properties of the resulting aggregates are mainly stochastic, however interesting patterns can be identified. This study matches estimated macro-porosities of S-type asteroids and finds a loose linear relationship between macro-prorosity of asteroid aggregates and the mass ratio of the largest component to the whole aggregate (for both S and C-types). As for observed C-type asteroids, we conclude that their interiors should be more fragmented than in the case of S-type asteroids, explaining the difference in the estimated macro-porosity of real C asteroids with respect to S-types. We also find that slow rotators may be interpreted as a natural result in the process of gravitational reaccumulation.

1. Introduction

Despite major improvements to asteroid research have been made in the last decades, no direct measurement of the internal structure of asteroids has been possible yet. A new era of space exploration of asteroids using instrumentation capable of measuring their interior structure is about to start but—at the moment—we only can rely on theoretical and statistical findings, indirect measurements and numerical simulations to understand the interiors of asteroids.

From a theoretical point of view, Jeffreys (1947) and Opik (1950) introduced the idea that some asteroids and comets may not necessarily be monolithic objects governed only by material solid state forces. Chapman (1978) used the term 'rubble pile' for the first time to indicate the result of the gravitational reaccumulation of boulders derived from catastrophic collisions on asteroids. 'Rubble pile' is used in planetary science and geology to describe a variety of configurations and may lead to some confusion regarding precise definitions. The Richardson et al. (2002) chapter in *Asteroids III* made an effort to standardize terms for asteroid structures consisting of multiple components kept together by self-gravity and they are properly referred to as 'gravitational aggregates' (GA) a terminology that we will adopt for the rest of this paper. Petit and Farinella (1993) showed that gravitational reaccumulation is indeed possible by calculating explicitly the balance between the gravitational binding energy and the kinetic energy of the fragments produced after catastrophic collision. The energy condition that they found is a function of a number of poorly known physical quantities, in particular of the critical shattering specific energy Q_S^*, which is the minimum energy per unit mass necessary to disrupt the parent body. Q_S^* has been estimated by laboratory experiments in the small size range of 10 to 20 cm targets for many different materials. Values for multi-km objects are derived by scaling theories and—alternatively—by numerical simulations mainly based on Smoothed Particle Hydrodynamics (SPH) and CTH (Combined Hydro and Radiation Transport Diffu-

* Corresponding author at: Departamento de Física, Ingeniería de Sistemas y Teoría de la Señal, Escuela Politécnica Superior, Universidad de Alicante, p.O. Box 99, Alicante, 03080 Spain.
E-mail address: acb@ua.es (A. Campo Bagatin).

https://doi.org/10.1016/j.icarus.2017.11.024
0019-1035/

sion) codes (Love and Ahrens, 1996; Benz and Asphaug, 1999; Jutzi et al., 2010; Leinhardt and Stewart, 2009).

The threshold specific energy for dispersal is strictly related to the reaccumulation process itself and is indicated by Q_D^*. This is the specific energy necessary to disperse more than half of the mass of the target body. We restrict this introduction on Q_D^* to the case in which the mass ratio between the projectile and the target is small, which happens in the overwhelming majority of shattering events due to the exponential size distribution of asteroids involved in collisional cascades (Campo Bagatin et al., 2001, e.g.). Notice that Q_S^* and Q_D^* are different. They are essentially the same in the strength regime, that is in the size range at which self-compression and self-gravity are not important (below some 100 m). In the gravity regime, instead, they take different values ($Q_S^* < Q_D^*$) due to the fact that Q_S^* is essentially increased only by self-compression as size increases, while Q_D^* is furtherly increased by self-gravitational energy between components. That makes the target much harder to disperse than to shatter (Holsapple et al., 2002).

Campo Bagatin et al. (2001) developed algorithms based on the Petit and Farinella (1993) study to calculate and keep track of the amount of reaccumulation occurring in any possible collision and applied it to the numerical simulation of the collisional evolution of the main asteroid belt. They found that a significant fraction (50 to 100%, depending on different physical assumptions) of objects in the 10–100 km size range are expected to be gravitational aggregates.

In this work, we introduce a new approach to the study of asteroid internal structure, based on laboratory fragmentation experiments (Durda et al., 2015) combined with numerical simulations using the code *pkdgrav*, a package extensively adopted to deal with *N*-body problems in planetary science. In particular, we exploit the possibility to make irregular rigid structures with *pkdgrav* and follow their dynamical and collisional evolution to gravitational aggregate end states. Section 2 is a short summary of the observational evidences for the existence of GAs. Section 3 introduces the basic parameters used to characterize the internal structure of asteroids. A brief summary of the work developed in the past on the same topic is in Section 4. The detailed explanation of the method used is in Section 5 and the corresponding results in Section 6. A discussion of the results (Section 7) and the conclusions (Section 8) close the paper.

2. Observational evidences for gravitational aggregates

The possibility that most asteroids ranging from a few hundreds of meters to around a few hundreds of km in size are GA has gained acceptance. The reason for this is mounting observational evidence, largely discussed in Richardson et al. (2002), which we shortly summarize here.

2.1. Low bulk densities

Few direct mass and shape measurements have been performed: C-type asteroid Mathilde (*Galileo* space probe) (Cheng, 2004)) and S-type asteroids Eros (*NEAR* space mission) (Cheng, 2002, 2004) and Itokawa (*Hayabusa* space mission) (Yoshikawa et al., 2015, and references therein) were characterized by spacecraft observations. Those measurements together with multiple radar observations of binary NEAs and optical and NIR observations are providing reliable estimations of bulk densities for a statistically significant number of asteroids. Another way to get a mass is to measure the Yarkovsky effect as was done for, e.g., Bennu, the *OSIRIS-REx* mission target (Chesley et al., 2014). Together with ground-based observations of the size, Bennu's density was estimated. One of the most striking findings in close observation and measurement of asteroids' masses and sizes is their apparent low densities. S- and C-class asteroids show lower mass densities with respect to their corresponding meteorite analogues (Carry, 2012). For example, the density of S-type Asteroid Itokawa was estimated to be 1.9 g/cm^3 and that of C-type Mathilde 1.3 g/cm^3, clearly smaller than their corresponding analogue meteorites, respectively around 3.0–3.5 g/cm^3 for ordinary chondritess and 2.0–2.5 g/cm^3 for carbonaceous chondrites. The measured density of Itokawa is consistent with about 40% void space (Abe et al., 2006).

2.2. Fast rotation

Measurement of asteroid spin periods from lightcurve analysis have placed constraints on asteroid properties. There apparently is a sharp cutoff around 2.2 h for the spin period of asteroids; very few asteroids larger than 200 m have been observed spinning faster than this limit (Pravec and Harris, 2000). There is no reason a priori why a monolothic body would be precluded from spinning faster, suggesting that most asteroids larger than 200 m have no tensile strength. That can be explained if they are made of components kept together by self-gravity. Holsapple (2007) showed that some little tensile strength—mainly due to cohesion forces between components—is necessary to explain the fastest observed spin periods even below 2.2 h.

2.3. Giant craters

Besides martian satellites Phobos and Deimos (possibly asteroids captured by planet Mars), most asteroids directly imaged to date (e.g., Gaspra, Ida, Mathilde, Eros, Steins, Lutetia, Steins) have craters with large diameters, in some case as large as the radius of the object itself (Chapman, 2002; Michel et al., 2015). Asphaug (1999) showed numerically that such features can be explained by the absorption of part of the impact energy by a GA structure. A monolithic asteroid would not withstand collisions able to produce those craters: they would be completely shattered and dispersed in most cases.

2.4. Crater chains

Linear configurations of up to tens of equally spaced, similarly sized impact craters that spread out over tens of kilometers have been observed on the surface of planets and satellites. Melosh and Schenk (1993) and Bottke et al. (1997) have suggested that these catenae are impact signatures of fragment trains belonging to tidally disrupted GAs, though attributed to comets in many cases.

2.5. Grooves

Linear depressions have been observed on every asteroid for which high-resolution images of the surface have been obtained (Thomas and Prockter, 2010). They are currently believed to form where loose, incohesive regolith drains into underlying gaping fissures. The fissures may not have been initially formed by impacts, but they probably open every time a large impact jostles the interior of the asteroid, so the grooves may postdate the fissures themselves. The presence of grooves on an asteroid thus suggests that its interior may be somewhat coherent but fractured.

2.6. Asteroid Itokawa

The most striking evidence of the existence of GAs probably is the observation of asteroid 25143 Itokawa. This small and irregular ($\approx$ 500 m $\times$ 300 m $\times$ 200 m size) S-asteroid—that was visited by the Hayabusa spacecraft in 2006—shows many features that can

be suitably explained by a GA structure. Boulder blocks as large as those found on Itokawa could not have formed as cratering impact ejecta on a body of this asteroid size, and the volume of mobile regolith estimated on Itokawa is too great to be consistent with any cratering activity. Itokawa's volume of gravel-sized regolith is consistent with extrapolation of its boulder size distribution (Saito et al., 2006; Miyamoto et al., 2006), suggesting a fragmentation size distribution. Those observations can be explained by a catastrophic disruption scenario for the formation of Itokawa followed by the reaccumulation of part of the formed fragments. Nevertheless, the interior of Itokawa may contain intact fragments that exceed 100 m size.

3. Characterization of the internal structure of gravitational aggregates

Campo Bagatin et al. (2001) and Richardson et al. (2002) defined a gravitational aggregate as an object formed by many components. GAs are often associated with the reaccumulation of fragments of some former catastrophic collision, and they were defined in such a way that the mass of the largest one (M_{LF}) is not larger than half of the mass of the whole object (M), $f_{LF} = M_{LF}/M \leq 0.5$. That means that most of its mass is made of multiple single components randomly piled up by gravity. Unless aggregate structures at km size range were primordial in the Solar System, a circumstance for which no evidence is shown, we will consider them as the result of catastrophic fragmentation in the collisional evolution of the Main Asteroid Belt. f_{LF} relates to the relative kinetic energy of the impact (E) that produced the fragmentation that was at the origin of the reaccumulated body and to the threshold energy needed for the shattering of the target (Q_S^*), $f_{LF} \propto (Q_S^*/E)^{\alpha}$, where $\alpha = 1.24$ according to Fujiwara et al. (1977) experiments. Finally, f_{LF} is also related to the exponent of the cumulative mass distribution of the fragments generated in a given collision $N(>m) \propto m^{-\beta}$, with $\beta = 1 - f_{LF}$ (Petit and Farinella, 1993).

Relating mass and size ratios of components is not always straightforward nor intuitive. It is easy to check that in the idealized case of a threshold GA ($f_{LF} = 0.5$) of spherical shape, with a spherical largest fragment right in the core of the body, the radius of the whole structure would be just 26% larger than the radius of the monolithic core itself. The internal structure of a GA is not easy to characterize and the bulk mass density of an asteroid may provide a first clue to its structure. In fact, the bulk density of an asteroid can be compared to the density of meteorites that can be considered to be its analogue material based on spectroscopic observation of the asteorid itself. Precise measurements of meteorite densities are available and are summarized in Carry (2012).

Density is an indirect measurement itself which requires information about the mass of the asteroid and its volume. The mass can be estimated from close encounters with other asteroids and space probes or by analysing the orbit of a satellite in the case of binary asteroids (mostly among NEAs). It is much trickier to get reliable estimates of the volume of an asteroid as the shape needs to be derived together with a good estimation of its size. A comprehensive and updated discussion of those methods can be found in Carry (2012). It is worth remembering that the uncertainty on the estimation of these quantities can often be large. Unless measurements are a consequence of close space-mission-fly-bys or by detailed radar observations, volume estimates are very uncertain if derived from optical observations, as no knowledge of the shape is available and biases are possible in the determination of the albedo of the object itself, which affects size estimation. For that reason only a limited number of asteroids possess reliable estimations of their bulk density (Carry, 2012).

Some information on asteroid structure can be derived through the interpretation of its porosity, which is meant in this context as the void space left between components within a given structure. This is usually referred to as *macro*-porosity in asteroid science, not to be confused with *micro*-porosity, which refers to the microscopic voids inside the structure of the analogue meteorites as measured on Earth, typically ranging from 0 to a few percent. In this work the term *porosity* will always refer to *macro*-porosity. This parameter is related to the material, ρ_m, and bulk, ρ_b, density:

$$P = \frac{total\ void\ space}{bulk\ volume} = 1 - \frac{\rho_b}{\rho_m} \tag{1}$$

Sometimes the term 'packing fraction' (*PF*) is used to define the fraction of volume occupied by solid components inside a given volume. This quantity is related to porosity as $P = 1 - PF$. Besides bulk density and porosity, the ratio of the mass of the largest component to the mass of the whole body (f_{LF}) may be useful to have an idea of what the structure of such a body is. We may hope to estimate this parameter on some asteroids by means of low-frequency radar measurements in the future.

Unfortunately, packing fraction (and therefore porosity) itself is a scale–invariant parameter, so the information on internal structure that can be inferred from it is reduced. It is easy to show that equal size spheres in a jar large enough to neglect wall effects will have the same packing fraction as smaller (or larger) spheres filling the same jar. The same happens for any other geometric solid and for equal size distributions of spheres (or other shapes). In this case the packing fraction only depends on the fractal dimension of the given distribution. The same packing fraction may correspond to a distribution of large boulders piled up by self-gravity and to a sand pile with the same size distribution. Therefore, even if porosity is very useful to understand a given structure, it provides no information about the texture of the structure itself.

A phenomenological attempt to characterize structural diversity was made by Richardson et al. (2002), who defined a *Relative Tensile Strength* (RTS) as:

$$\mathrm{RTS} = \frac{Tensile\ strength\ of\ object}{Mean\ tensile\ strength\ of\ components} \tag{2}$$

Based on porosity and RTS, Richardson et al. (2002) built up a characterization that may be useful to distinguish among objects with different physical structures and impact responses. However, we find that such a high level of analysis is premature as the amount of information available for the internal structure of asteroids to compare with is still limited. Therefore we will stick only to those parameters that may help to compare asteroid observables to numerical modelling.

Bulk density, ρ_b, porosity, P, and the largest component mass ratio, $f_{LF} = m_{LF}/M$, are therefore convenient parameters to study asteroid structure at the current level of knowledge.

4. Previous numerical work

Gravitational aggregates have been modelled in the past mostly as monodisperse collections of spheres. Often the *pkdgrav* code, a numerical package able to deal with the *N*-body problem and with collisions between particles has been used. As we adopted an updated version of this very code, it will be introduced later on with some detail. The effects of low-speed collisions between GAs have been studied in this way by Leinhardt et al. (2000) and—including the effects of rotation—by Ballouz et al. (2014, 2015) and—by means of a different code—by Takeda and Ohtsuki (2007, 2009). This kind of modelling—based on Hard Sphere Discrete Element Model—has also been used to understand the tidal effects (Richardson et al., 1998) and the formation of binary asteroids assuming aggregate structures again as collections of monodisperse

(Walsh and Richardson, 2006; Walsh et al., 2008) and multidisperse spheres (Walsh et al., 2012), as well as the shapes of asteroids under different spin states (Richardson et al., 2005; Tanga, 2009). A similar—Discrete Element Model (DEM)—numerical approach, including inter-particle van der Waals forces, Sanchez and Scheeres (2012) studied the effect of rotational spin up on multidisperse spheres GAs with cohesion. Michel et al. (2001, 2002, 2004), Durda et al. (2004, 2007) and Benavidez et al. (2012, 2017) applied *pkdgrav* to the outcome of SPH codes to reproduce cratering and shattering events, so that they could follow the evolution of the ejected fragments. The code assumes spherical fragments as created by the SPH and merged them again into spherical particles as they collide at low speeds. In that way, they studied in a comprehensive way the size distribution of many asteroid families, reproducing them successfully in many cases.

Tanga et al. (1999) and Campo Bagatin and Petit (2001) used a different 'geometric' approach to understand asteroid internal structure: they made fragments grow from random seeds inside a given volume (the asteroid overall volume) until contact surfaces met. In this way, with no physics involved in the process, they managed to reproduce the size distributions of a number of asteroid families. The first attempts to abandon the idealized spherical approach for aggregate components were carried out by Korycansky and Asphaug (2006) who developed their own code and performed numerical experiments similar to those of Leinhardt et al. (2000) did, using polyhedral shapes for fragments in both monodisperse and multidisperse configurations. Richardson et al. (2009) and Michel and Richardson (2013) introduced cohesion forces in *pkdgrav* code so that the fragments produced during the SPH phase would just stick together instead of being merged into a new spherical fragment. That permitted random irregular shapes for the ejecta. These components then may aggregate by self-gravity, forming non-spherical objects.

5. Methodology

We introduce a new approach to the study of the internal structure of small bodies of the solar system considered as gravitational aggregates of irregular-shape components, and we apply it to small asteroids (500 m to 10 km equivalent diameter). We outline here the strategy that we adopt to study this problem; details will be given in the Sections 5.1, 5.2 and 5.3. The overall idea is to start our simulations once a given catastrophic collision has taken place, part of the fragments have escaped the system and the remaining fragments are starting to come back and reaccumulate under mutual gravitational interaction. We only worry about the accreting fragments and do not simulate the fate of escaping ones.

Former numerical studies investigated the outcome of catastophic disruption by means of SPH or CTH hydrodynamics codes and followed the dynamical evolution of the resulting fragments treated as spherical particles (see Section 4). We replace that step by using the outcome of a set of laboratory experiments of catastrophic fragmentation of basalt targets described in Section 5.1 (Durda et al., 2015). We use measurements of the experimental relative mass distributions (m_i/M, where m_i is the mass of a given fragment and M the mass of the target) to get the mass distributions of the synthetic components of our numerical simulations. Given the chosen asteroid size range (500 m–10 km) to be simulated, in our case there is no need to scale the results of laboratory experiments according to scaling laws for the threshold specific energy for fragmentation (Q_D^*) to obtain the corresponding mass distributions. The $Q_D^*(=Q_S^*)$ values of our laboratory sample targets ($Q_S^* = 800$ J/kg for targets around 7 cm equivalent diameter impacted at 15 deg with respect to the normal direction) corresponds roughly to the Q_D^* in the chosen range of simulations (1–10 km) for most of the scaling-laws frequently used in asteroid modelling (Love and Ahrens, 1996; Melosh and Ryan, 1997; Benz and Asphaug, 1999; Jutzi et al., 2010) as can be seen in Fig. 1. This may seem surprising but is a consequence of the behaviour of the scaling-law profiles derived theoretically and numerically for Q_D^* as a function of size. In principle, scaling-laws allow for this operation, however, no real experiment has been carried on so far at asteroid scale, and we have to assume as an ansatz that the fragmentation properties are similar for the asteroids as for the lab-scale experiments.

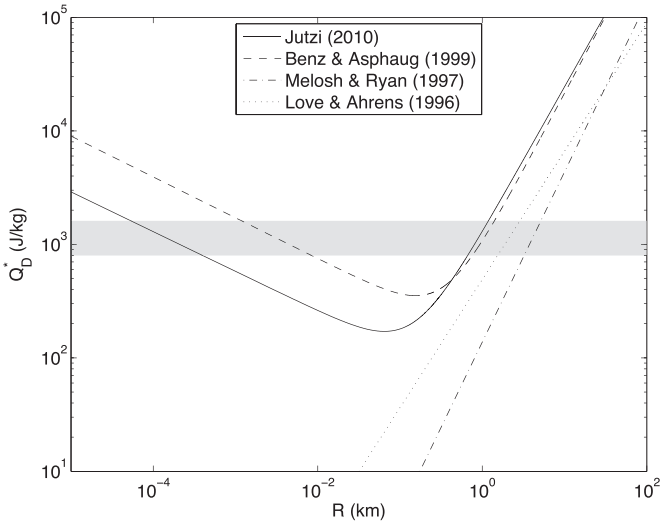

Fig. 1. Scaling laws for Q_D^* compared with experimental values of the basalt target samples used at NASA Ames experiments (Durda et al., 2015). The gray band stands for Q_S^* experimental values corresponding to different impact angles.

The threshold energy for shattering decreases with size in the strength regime until self–compression due to gravity and self-potential energy make targets harder to shatter and disperse at increasing size.

The governing parameter of the slope of the mass distribution is the fraction of the largest fragment to the target mass, f_{LF}, and this in turn depends on Q_S^* and on the specific collision energy Q. If both are very close to the actual values for asteroids, the experimental results are going to be the same in terms of relative mass distribution and can be translated to real asteroid scale at the given range.

Therefore, we build our synthetic fragments—for any given simulation—by making a set of rigid aggregates using *pkdgrav*. The mass distribution and the shapes of the fragments are drawn at random from the mass distribution and from the distribution of size ratios of the fragments measured in laboratory experiments (Durda et al., 2015). Finally, we place our fragments in space at random positions, with random velocities directed towards the centre of mass and with random spins, then let *pkdgrav* evolve them until they form a gravitational aggregate. We consider that the aggregate has stabilized when the kinetic energy of its components reaches asymptotic values. At that point we measure its main physical parameters: bulk density, volume (therefore its porosity), elongation and spin state. This process is explained with full detail in the following subsections.

5.1. Fragmentation experiments (Durda et al., 2015)

The starting point of the methodology used in this work is the results obtained in the set of impact and fragmentation experiments carried out in July 2013 at the NASA Ames Vertical Gun Range (AVGR) facilities, in Mountain View (California, USA). The results of those experiments were published in Durda et al. (2015) and they were taken as the basic standard to build the rigid aggregates that will be the basic components of our

simulations of gravitational re-accumulation. The outcome of six high-speed (4 to 5 km/s) collisions on three spherical and three irregular basalt targets were analysed, the mass of hundreds of fragments created in the collisions were measured and the corresponding mass spectra for each catastrophic impact were represented by cumulative mass distributions characterized by a power-law of the form:

$$N(>m) \propto m^{-\beta} \tag{3}$$

where $N(>m)$ is the number of particles larger than a given mass m and the exponent β ranged from 3/4 to 5/4. That was in agreement with most past experimental studies of fragmentation in hyper–velocity regime carried out since the eighties by different researchers (Holsapple et al., 2002). In this sense, the mass–frequency distributions found by Durda et al. (2015) have nothing unusual about them with respect to many previous impact experiment studies. We make reference to them to be consistent with the fragment shape distributions taken from that work. The shapes of each of the largest 36 fragments corresponding to each fragmentation experiment were accurately measured, so that they could be characterized by the length of 3 characteristic orthogonal axes. The average size ratios $(b/a, c/a)$ were found to be 0.7 and 0.4 respectively. In this way we obtained 6 sets of largest fragment mass ratios (f_{LF}), mass distributions (exponent β) and fragment shapes for the largest 36 fragments (Durda et al., 2015). Those experimental results are used in this work to randomly select mass distributions and shapes of fragments in the numerical simulations performed by *pkdgrav*.

5.2. pkdgrav: *A numerical package for* N-*body interactions*

In order to carry out our numerical simulations of gravitational reaccumulation, we use the *pkdgrav* code, a package created at the University of Washington for cosmological modelling (Richardson et al., 2000). It is basically a program designed to calculate gravitational interaction in *N*-body problems, including a complete treatment of all kinds of elastic and inelastic collisions (Richardson et al., 2000; Stadel, 2001). Some of the applications to solar system research have been summarized in Section 4. Recently, the code has been updated to relax the *hard-sphere* approach and move to a *soft-sphere discrete element method (SSDEM)* (Schwartz et al., 2012). We utilize this latest version of the code in all numerical simulations. This model conserves angular momentum but permits energy dissipation according to the selected material parameters. In the soft-sphere approach, particles are permitted to overlap very slightly (typically less than 1% of the radius of the smallest particle) so that restoring and frictional forces may be applied in proportion to the overlap. In other words, we are modelling the contact physics explicitly, using an approach developed in the granular physics community (Cundall and Strack, 1979). The approach accounts for dissipation using coefficients of restitution, and frictional forces arising from relative sliding, rolling, and twisting motions at the contact point, each parameterized by dimensionless coefficients. We used values appropriate for "gravel-like" material, based on Yu et al. (2014). More details of the implementation are provided in Schwartz et al. (2012).

The *pkdgrav* feature that we exploit in this work is the possibility to model the behavior of bound (rigid) aggregates, represented as sets of unbreakable spheres whose mutual offsets are forced to be kept constant so that the whole aggregate moves as a single rigid solid. Thus, the code deals with each of these rigid aggregates as individual bodies, calculating the position and velocity vectors of each mass centre and the corresponding inertia tensors. These aggregates obey the Newtonian equations of motion, along with the Euler equations for the rigid body (Richardson, 1995; Richardson et al., 2009). Such aggregates are also rigid in the sense that they cannot deform nor break. When a collision between aggregates takes place, the results are constrained by the parameters the user previously defined in an input file. These parameters include the degree of energy dissipation and the mechanical results when particles bounce after colliding, according to normal and tangential restitution coefficients, the coefficients of friction between surfaces and the elasticity coefficient controlling the amount of overlapping between spherical components in the soft sphere model.

The integration time step of a given simulation and the elasticity coefficient are chosen to ensure that particle overlaps do not exceed 1%, based on the range of particle sizes, aggregate masses, and encounter speeds characteristic of each simulation. Excessive overlaps trigger warnings or, in extreme cases, run failure, as a safety feature.

Other parameters of special relevance, such as the normal (ε_N) and tangential (ε_T) restitution coefficients (the ratio between speed in a given direction after and before collision) are chosen by the user and they may range from 0 to 1. In preliminary tests the results of simulations have been shown to be essentially insensitive to ε_T when larger than 0.6. Instead, results are more sensitive to the choice of ε_N. We took into account estimations for rocks and trends for ε_N in experimental studies showing that this parameter tends to take smaller values for coarse spheres as compared to smooth spheres of the same material (Durda et al., 2013). Our set of nominal values is $(\varepsilon_N, \varepsilon_T) = (0.3, 0.8)$. However we checked our results against major changes in ε_N (see Section 6.6.2). Suitable values were chosen for sliding friction ($\mu_s = 0.5$), rolling friction ($\mu_r = 0.1$) and twisting friction ($\mu_t = 0.1$) coefficients. Time step and elasticity coefficient were respectively in the following ranges: δ=$(4.45\times10^{-3},\ 5.93\times10^{-3})$ s and k_n=$(3.045\times10^{14},\ 1.37\times10^{16})$ kg/s^2, depending on the mass and scale range of the initial conditions of the systems to be simulated.

5.3. Numerical simulations

The mass and shape (axis ratios) distributions obtained in the experiments described in Section 5.2 were the starting point from which random distributions of masses and shapes of the synthetic fragments (often 'components') were built for numerical simulations.

From each of the six collisional experiments at NASA AVGR, we worked out a relative mass (m_i/M) distribution and the aspect ratios for the largest 36 fragments. We label our experiments as *shot1, shot2, shot3, shot4, shot5* and *shot6*, corresponding to the 6 sets of experimental results.

For any given simulation we draw at random a number of fragments from the corresponding experimental distribution. We decided to limit that number to 36 to match the number of measured shapes and in order to avoid having too many particles in the simulations that would have increased computing time. This gives us a range for the total number of particles in each simulation between $\approx$4000 and $\approx$10000. Those 36 largest fragments represent 29% to 68% of the volume of the experimental targets, depending on the considered shot. That covers a wide range of possible asteroid shattering events for which part of the mass would be dispersed (71% to 32%) and the rest will reaccumulate by self-gravity. This choice is also justified by the fact that large fragments usually have the lowest ejection speeds in catastrophic fragmentation (Nakamura and Fujiwara, 1991; Giblin, 1998) and are more likely to be reassembled in the reaccumulation process than fines.

We build our synthetic irregularly shaped components out of a *mother* sphere which is obtained by randomly assembling a cloud of 5000 spherical particles by self-reaccumulation (Fig. 2). Each component is a rigid aggregate made of spherical particles (Section 5.2) and it has a temptative 3D ellipsoidal shape whose axes ratios are randomly taken from the experimental distributions

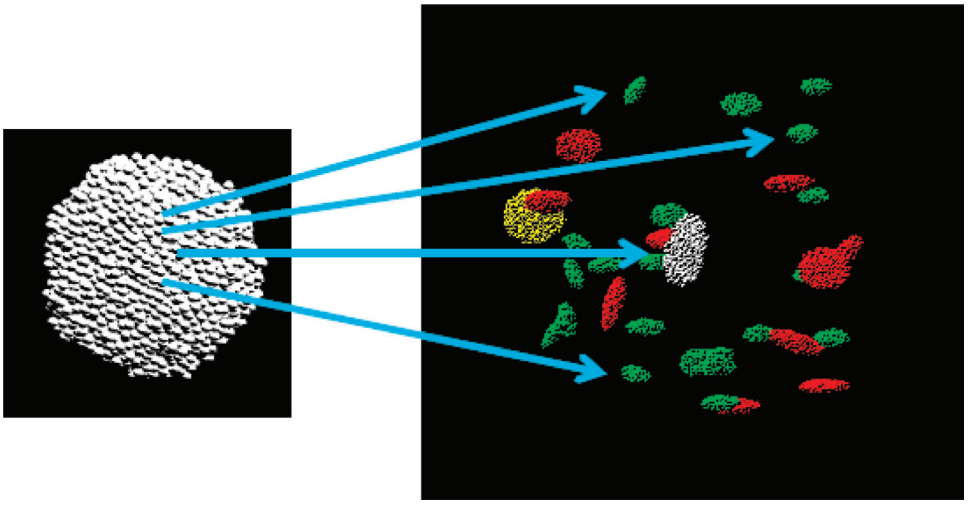

Fig. 2. The algorithm extracts components from a mother-cloud with 5000 particles. The colour code (online version) corresponds to mass ratio ranges, m_i/m_{LC}. m_i is any component mass, m_{LC} is the mass of the largest component of the aggregate. m_i/m_{LC} correspond to 1 (white), 1/2 (yellow), 1/4 (red), 1/8 (green), 1/16 (b lue). (For interpretation of the references to colour in this figure legend, the reader is referred to the web version of this article.)

described in Section 5.1. A given density is assigned to the whole sphere and that is the density of the components. For the sake of simplicity we only considered two nominal densities: 3500 kg/m^3 and 2500 kg/m^3, approximately corresponding respectively to average values for ordinary chondrites, assigned to be meteorite analogues of S-type asteroids, and to carbonacous chondrites, assumed as meteorite analogues of C-type asteroids.

The way fragments are extracted and distributed into space under certain boundary conditions (relative distance between components, overall volume, initial velocity and spin vectors, initial angular momentum) is controlled by the program *cumulatur*, an *ad hoc* algorithm developed by the group at University of Alicante.

For any of the experimental distributions, we first of all maximize the size of the largest fragment so that it occupies the maximum volume inside the *mother*-sphere, in order to have the best available resolution. For the rest of the fragments we draw at random mass ratios m_i/m_{LF} from the corresponding relative mass distribution and sets of aspect ratios from the values obtained from the empirical distributions of shapes. In this way we have a different set of three values for axes ratios associated with each mass ratio. This procedure can be repeated as many times as needed depending on the number of components to be built. Finally the whole distribution is scaled to a convenient size, keeping the density of components constant. Our nominal case is such that the group of all components together has an equivalent spherical diameter of $\approx$2 km.

In order to check the validity of our results over different scales, simulations were run changing the scale of the whole system in such a way that the final aggregates were set to be approximately 0.5 km and 10 km in equivalent diameter, respectively (Section 6.6.1). In any given simulation, components have to be located in space under suitable boundary conditions. The largest component of the distribution is placed at the centre of the coordinate system and the rest are randomly located in space freely or within a given limiting volume. Overlaps are avoided in the set up process by spacing components suitably.

Different values for the limiting overall volume have been considered to check the dependence of the results on boundary conditions. We take, as unit size for the radius of the boundary volume sphere within which synthetic components may be distributed, the radius R_e of the equivalent sphere of volume V_e containing the mass of all the components in each simulation. We choose as possible values for the sphere radii the sequence of values $2.000 \cdot R_e$, $3.175 \cdot R_e$, $4.000 \cdot R_e$ and $5.045 \cdot R_e$. This choice corresponds to boundary sphere volumes that double with respect to each other so that $V_4 = 2V_3 = 4V_2 = 8V_1 = 16V_e$.

A radial velocity directed towards the centre of mass and a spin vector are assigned randomly to every component within given ranges. The velocity distribution is taken as uniform up to values smaller than the escape speed (typically a few tens of cm/s for km-size objects, depending on the mass of the system). Our initial conditions are a snapshot of the dynamical situation of the fragments that are bound gravitationally, once they have inverted the direction of their velocity vector and are on their way back to the centre of mass of the system. Nobody knows what the velocity distribution is at that point. Moreover, fragments do not invert the direction of velocity at the same time. Assuming any kind of distribution at a given time is indeed arbitrary, so we chose a simple uniform distribution of speed values. No mass-velocity dependence is assumed in this phase.

The rotation period of each component was drawn from a flat distribution centered on 6 h average spin period in the range 0–12 h. Again, there is little knowledge on the spin distribution of fragments coming out from shattering experiments, therefore any assumption is arbitrary. Main Belt asteroids are collisionally evolved, which causes their spin periods to approximately match a Maxwellian distribution (Farinella et al., 1981) centred at about 6 h. In our case, the spin distribution coming out of shattering events is not necessarily non-uniform and certainly not collisionally evolved. Therefore, we assumed a simple flat distribution for the spin rates of components within the range mentioned above, centered on the average value of Main Belt asteroid spin rates.

Once radial velocities and spins are assigned, it is possible to change the value of the overall angular momentum to match specific situations. In this way, we are simulating the initial conditions of a mass distribution of fragments with irregular shapes that are at the beginning of the reaccumulation phase following a catastrophic disruption where the fragments with ejection speeds larger than the escape limit have already left the system.

pkdgrav allows the system to gravitationally and collisionally evolve until stabilization. When the simulation is over, volume, density, porosity and elongation are calculated by a suitable algorithm (*bulkvol*) developed for this purpose in the frame of this research.

Elongation is a measure of off-centre mass distribution of the reaccumulated body and is calculated as the distance between the position of the centre of mass of the largest component, $\vec{r}_{LC}$, and

the position of the centre of mass of the rest of components, $\vec{r}_{RC}$, normalized to the radius of the equivalent sphere of the aggregate (the sphere whose volume is equal to the volume of the aggregate itself), R_e.

$$E = \frac{|\vec{r}_{LC} - \vec{r}_{RC}|}{R_e} \tag{4}$$

Alternative metrics for elongation are possible, but we rather wanted to highlight the asymmetry of the final distribution with respect to the position of the largest component. In this way, a roundish body with its largest component on one side of it will have a larger elongation than a similar shaped body with its largest component in the centre of the structure.

The determination of the volume V_b of a reaccumulated body is an inherently complex problem because the surfaces of GAs are hard to define. However it is possible to estimate them with different techniques and we finally chose the DEEVE (Dynamically Equivalent Equal Volume Ellipsoid) method, widely used for the calculation of the volume of irregular bodies in observational surveys.

This method is based on a general result that equates the volume of any rigid solid with that of the triaxial ellipsoid whose axes coincide with the principal axes of inertia of the solid itself. Formally it is necessary to calculate the inertia tensor of the reaccumulated body with respect to a system of axes located in the centre of mass of the system. The eigenvalues of this tensor are the principal moments of inertia of the rigid solid (I_{xx}, I_{yy}, I_{zz}) in the body frame. The inertia tensor of a triaxial ellipsoid is a diagonal matrix and there is a direct relation between its axes length (α, β, γ) and the principal moments of inertia of the rigid solid. For the ellipsoid to be dynamically equivalent to the rigid solid, the moments of inertia of the ellipsoid and the solid must be equal. When that requirement is satisfied, the volume of the ellipsoid is equal to the volume of the rigid solid itself, no matter how irregular the shape of the body is.

The principal moments of inertia can be expressed for a triaxial ellipsoid in terms of its spin axes and total mass M:

$$I_{xx} = \frac{M}{5}\left(\beta^2 + \gamma^2\right)$$

$$I_{yy} = \frac{M}{5}\left(\alpha^2 + \gamma^2\right)$$

$$I_{zz} = \frac{M}{5}\left(\alpha^2 + \beta^2\right)$$

where α, β, γ can be worked out from the previous relationships and the volume of the triaxial ellipsoid equal to that of the rigid solid is:

$$V = \frac{4\pi}{3}(\alpha \cdot \beta \cdot \gamma) \tag{5}$$

Specifically, this calculation was done by rotating each aggregate so that its principal axes of inertia overlap the axes of the space frame defined by *pkdgrav* and calculating the corresponding moments of inertia I_{xx}, I_{yy}, I_{zz}.

Porosity was already defined in Section 3 and in this context it can be calculated as $P = 1 - (\rho_b/\rho_m)$, where ρ_b is the bulk density of the object, and ρ_m is the density of its single components. This parameter is equivalent to the percentage of void space in a body's volume. Taking V_b as the bulk volume of the object and V_v as the volume corresponding to all empty spaces inside the aggregate, the formal definition of porosity can be expressed as $P = V_v/V_b$.

This procedure is repeated for most simulations performed using two choices of bulk density. One such series, corresponding to S-type asteroids, uses components with a density of about 3500 kg/m^3, similar to the average value for meteorites in the class of ordinary chondrites, made mostly of silicate minerals. In the other series, corresponding to C-type asteroids, we work with components whose density is similar to that of carbonaceous chondrites, about 2500 kg/m^3.

The spin period of any final aggregate is given as an output of the *pkdgrav* code itself and the elongation is eventually calculated for the final structure.

6. Results

The results of the numerical study that we carried on may depend on a number of different boundary conditions, such as the total mass of the system, the volume occupied by the initial distribution of components at the very beginning of the reaccumulation phase, the density of components, the shape and mass distribution and the angular momentum of the system. As our main interest is the internal structure of small asteroids, in particular NEAs, our nominal case corresponds to a mass such that the reaccumulated body is about 2 km in diameter, considering single components with density 3500 kg/m^3 (nominal case, corresponding to S-type asteroids). Simulations to check the applicability of our results to other size ranges have been performed as well and the results are shown in Section 6.6.1. As previously discussed, our starting point is the set of former laboratory impact experiments. Six shots were performed at that time, but we recovered complete shape and mass distribution for 5 of them, namely *shot1, shot2, shot3, shot4* and *shot5*. Each experiment resulted in its own f_{LF} and mass distribution from which the synthetic mass distributions are randomly generated. Each random distribution itself is characterized by the ratio of the mass of the largest of the 36 components considered to the mass of the whole generated structure. We name this $f_{LC} = m_1/M$ to distinguish it from f_{LF}. To make this clear let us just recall that f_{LF} is the fraction of mass of the largest fragment with respect to the target mass. f_{LC} instead is the fraction of mass of the largest component of the aggregate structure with respect to the mass of the aggregate itself. These mass fractions make reference to two different objects: the target is the parent body before an impact takes place, while the aggregate is the object formed after the impact occurs (with loss of part of the target's mass) and gravitational reaccumulation takes place. The outcome of our simulations is described in terms of density, ρ (kg/m^3), porosity, P, spin period, T(h), and elongation, E, of the aggregate structure. In what follows we first describe two stages of our simulation runs: *Stage 1* and *Stage 2* differ mainly in the fact that in *Stage 1* the components are set at random in space without any specific limiting volume, while in *Stage 2* the limiting volume is the main boundary condition for the simulations.

Each simulation typically takes about two weeks of CPU time to complete on each of our 16 processors at clock frequency of 2.7 Ghz. Typical reaccumulation times for our collapsing structures to stabilize are between 3 and 5 hours of real time. This may be compared to the theoretical *free-fall* time of the same mass spread over some typical initial volume so that mass density is ρ, which is $t_{ff} = 66430/(\rho^{0.5}) \simeq 2$ h (where ρ is in kg/m^3). Our structures take longer than t_{ff} to settle down due to multiple damped rebound of the components.

We do not report our findings on the morphology of the diverse aggregate structures obtained in this research. That will be the main topic of a forthcoming paper.

6.1. Stage 1

We started our sets of numerical simulations by running 8 simulations per each experimental shot, that makes 40 simulations.

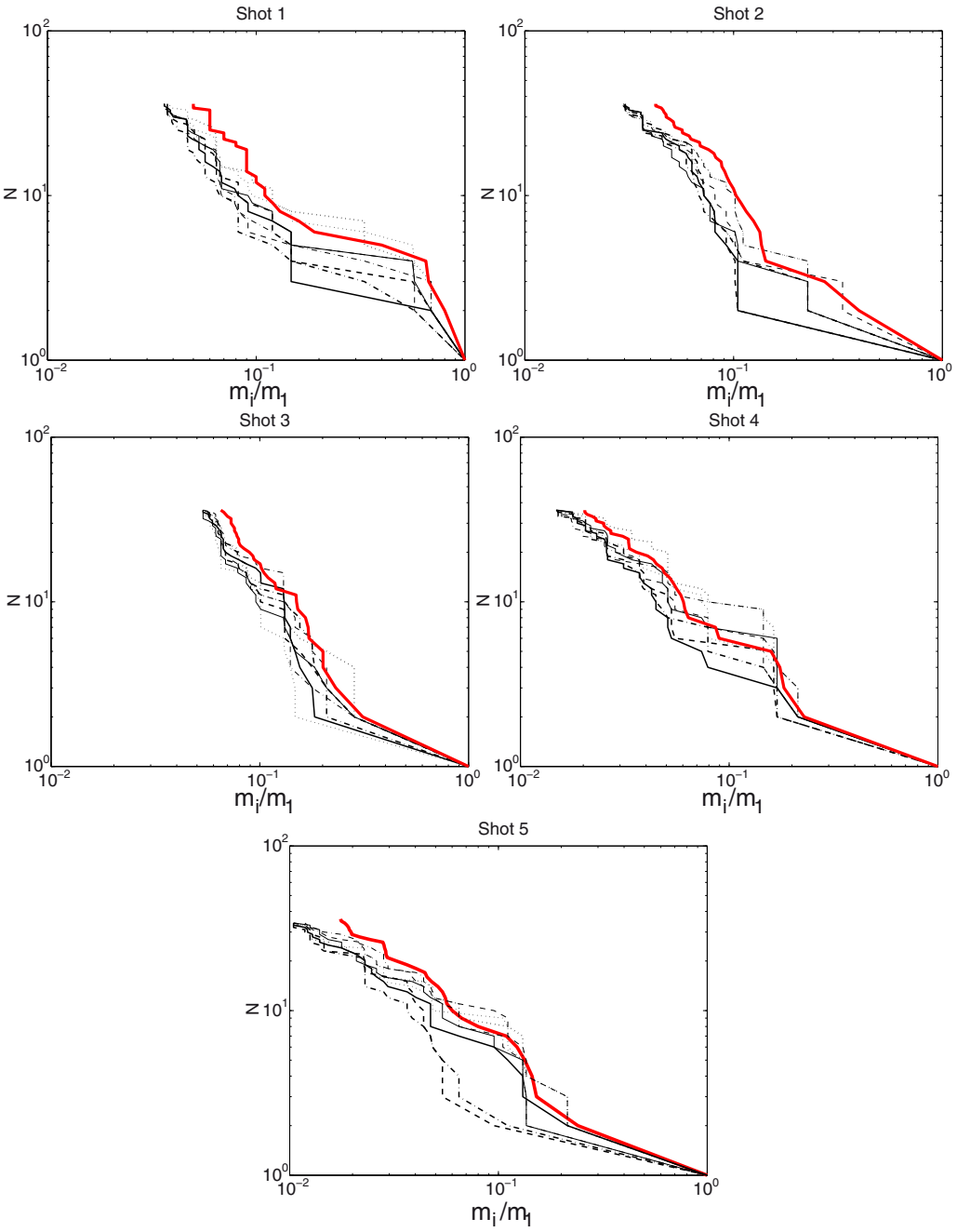

Fig. 3. Cumulative relative mass frequency distributions of the synthetic components of simulations in *Stage 1*. The gray (online: red) line is the corresponding experimental shot mass frequency distribution. The 8 synthetic distributions on each panel are not labelled as they correspond to random distributions with no specific characteristics. (For interpretation of the references to colour in this figure legend, the reader is referred to the web version of this article.)

As for the boundary volume conditions at this stage, for each simulation, the synthetic components were set at random in space at the beginning with the only condition that no component was set farther away from the centre of mass than 8 times the radius of the ideal equivalent sphere formed by all the components. For each shot, the cumulative relative mass spectrum of the synthetic components is shown in Fig. 3 with the relative mass distribution of the corresponding fragmentation experiment.

Table 1 reports the results obtained in the described set of simulations. Specifically, beyond the input parameter f_{LC}, the normalized angular momentum, $NAM = L/(GM^3R)^{1/2}$, the bulk density of the aggregate structure (ρ), its porosity (P), rotation period (T) and elongation (E) are reported.

At any stage of this research, some of the simulations did not result in aggregates within our standard CPU times, due—in most cases—to an excess of angular momentum of the system leading to temporary dispersion of a significant part of the structure. Those cases are indicated as 'N.R.' which stand for 'Not Reaccumulated'. Due to CPU time restrictions, these long-term evolution system evolutions had to be excluded from our results.

Table 1
Simulations corresponding to *Stage 1* (S-type typical density), where numerals from 1 to 8 label the simulation run for each shot. ρ (density in kg/m^3), f_{LC} (mass fraction of the largest component to the whole mass of the structure), *NAM* (normalized angular momentum), *P* (porosity), *T* (rotation period in hours), *E* (elongation), *N.R.* indicates that the structure was 'not reaccumulated' (see text).

Shot		Simulation							
		1	2	3	4	5	6	7	8
	f_{LC}	0.2511	0.2249	0.1689	0.2142	0.2038	0.2171	0.1734	0.2658
	NAM	0.1786	0.0480	0.0381	0.0489	0.0651	0.0608	0.0292	0.1531
Shot1	ρ	2121	2131	2266	2304	2421	2651	2441	2518
	P	0.4140	0.4114	0.3746	0.3639	0.3316	0.2679	0.3261	0.3041
	T	3.730	10.60	12.21	21.00	5.830	4.840	21.40	3.030
	E	1.7311	1.7599	1.2348	1.4281	0.8612	0.6846	0.3527	1.0028
	f_{LC}	0.3145	N.R.	N.R.	0.3096	N.R.	0.2809	N.R.	0.2727
	NAM	0.0977	N.R.	N.R.	0.0520	N.R.	0.0874	N.R.	0.0477
Shot2	ρ	2492	N.R.	N.R.	2385	N.R.	2098	N.R.	2296
	P	0.3091	N.R.	N.R.	0.3389	N.R.	0.4189	N.R.	0.3641
	T	5.460	N.R.	N.R.	4.170	N.R.	4.650	N.R.	5.270
	E	1.0403	N.R.	N.R.	1.1011	N.R.	1.8110	N.R.	1.4957
	f_{LC}	0.2050	0.2281	0.2514	0.2179	0.2304	0.2228	0.2236	0.2139
	NAM	0.0381	0.1155	0.0359	0.0369	0.2575	0.2782	0.1194	0.0579
Shot3	ρ	2050	2113	2334	2158	2183	2186	2284	2294
	P	0.4287	0.4101	0.3475	0.3980	0.3906	0.3900	0.3628	0.3603
	T	35.10	14.10	20.10	26.00	43.60	25.90	6.370	11.10
	E	1.3087	1.4649	0.5761	1.4942	1.4169	1.3016	0.8740	0.5894
	f_{LC}	0.3620	0.3620	0.3829	N.R.	0.3520	N.R.	0.4720	N.R.
	NAM	0.3895	0.0110	0.0847	N.R.	0.1000	N.R.	0.1227	N.R.
Shot4	ρ	2470	2455	2654	N.R.	2473	N.R.	2314	N.R.
	P	0.3076	0.3116	0.2551	N.R.	0.3174	N.R.	0.3477	N.R.
	T	9.996	8.528	7.130	N.R.	8.590	N.R.	9.060	N.R.
	E	1.2940	1.3161	0.3677	N.R.	1.0356	N.R.	0.7645	N.R.
	f_{LC}	0.4568	N.R.	0.3394	N.R.	N.R.	0.3356	N.R.	N.R.
	NAM	0.0072	N.R.	0.4635	N.R.	N.R.	0.3263	N.R.	N.R.
Shot5	ρ	2507	N.R.	2288	N.R.	N.R.	2264	N.R.	N.R.
	P	0.2890	N.R.	0.3563	N.R.	N.R.	0.3630	N.R.	N.R.
	T	135.0	N.R.	23.91	N.R.	N.R.	4.532	N.R.	N.R.
	E	1.0077	N.R.	1.3623	N.R.	N.R.	1.5531	N.R.	N.R.

6.2. Stage 2

In order to check any influence on the results due to the volume of the initial distribution of the structure components, we performed a second set of numerical simulations, where we limited the boundary volume where components may be placed at random at the beginning of simulations. As described in Section 5.3, we chose 4 different initial boundary volumes (IBV).

The inspection of our parameter space implies again a large number of simulations. For this reason we decided to limit the total number of simulations and distribute them in multiples of 8 for operational reasons, on one hand, as we had 16 available processors on which the simulations had to be run. On the other hand, *shot1* and *shot3* resulted in very similar values of f_{LF}, and therefore redundant, so we decided not to run simulations corresponding to *shot1*. Therefore, 32 total simulations were run at this stage for each of the two values assumed for mass density of components, corresponding respectively to S and C-type asteroids.

In this way we mean to check if any dynamical difference is implied when changing mass density within a range of meaningful values in an asteroidal context. Finally, for any given case, two different simulations with different values of the angular momentum of the whole system were run, keeping all other boundary conditions constant (shape and mass distribution, location and velocity of components). The first set of runs have angular momentum values (CASE A) correspond to completely random values, while the second set (CASE B) is modulated in such a way that the resulting gravitational aggregate has a rotational period typical of NEAs in the studied size range (below $\approx$6 h).

Figs. 4 and 5 show the mass spectrum—in the case of S and C-type asteroids respectively—of each set of four different values of IBV corresponding to *shot2, shot3, shot4, shot5*, and the corresponding outcome.

Tables 2 and 3 report the results of each set of four different values of IBV corresponding to the same 4 shots and the corresponding outcome.

6.3. The spin period of gravitational aggregates

The histogram for the rotational period of the resulting aggregates is shown for all the simulations that were run with initial random values of the angular momentum of each system (Fig. 6), irrespective of the initial boundary volume of their components and their density. In this plot the 'forced' large angular momentum simulations are not included (CASE B in Tables 2 and 3). Histogram is shown for both S and C-type analogue mass densities. It shows an apparent concentration of values below 24 hours and a number of 'slow rotators', that is aggregates that have large rotational periods as a consequence of low values of the angular momentum of the system itself. This is shown in Fig. 7, where rotational periods are plotted as a function of the *Normalized Angular Momentum* (NAM). Values for rotational periods ranging from relatively fast spins (3.0 h) to periods longer than 24 hours (with a maximum value of 147.5 h) are found. The mean value of the whole distribution is 21.2 h, while the median is 10.6 h. The mean value for the periods of the reaccumulated bodies in the simulations is 9.8 h, when excluding from the calculation the bodies with rotation periods longer than 24 h.

When looking at the influence on rotational periods due to other boundary conditions, no correlation was found with their corresponding mass fraction f_{LC} nor the initial volume.

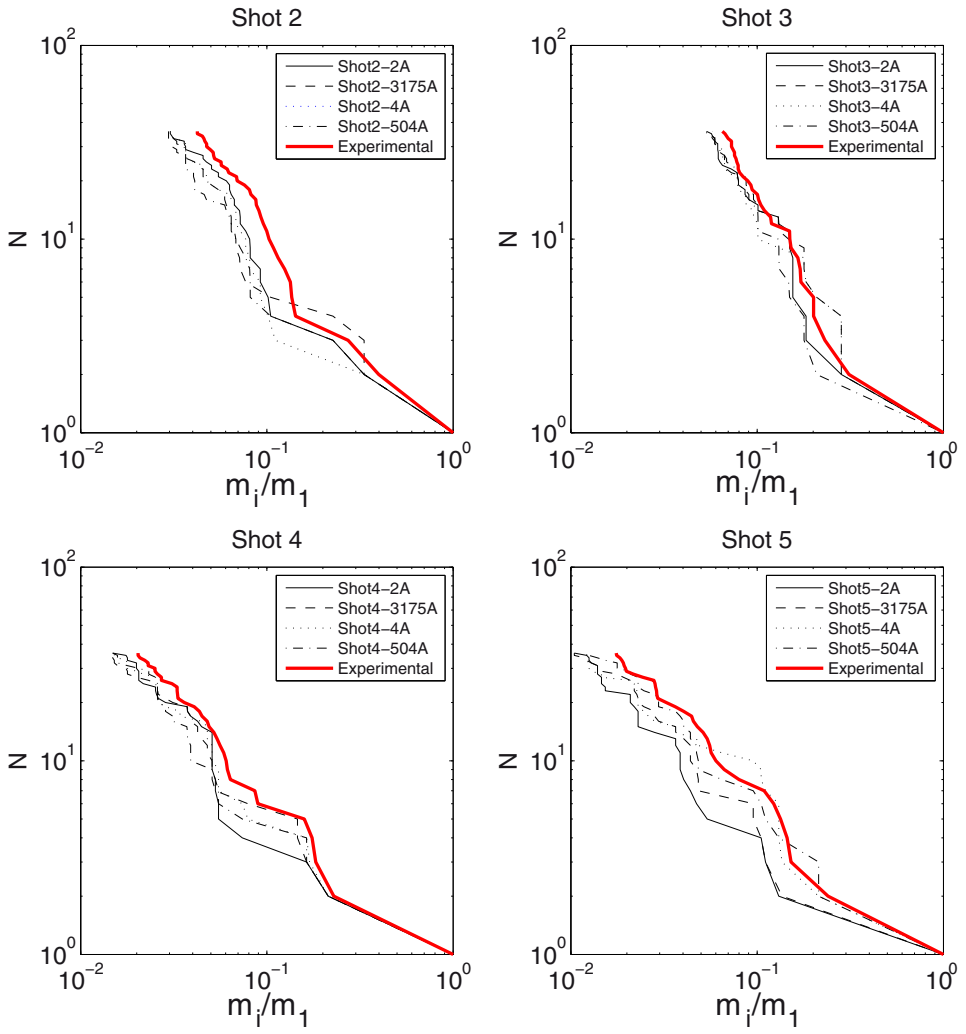

Fig. 4. Same as in Fig. 3 but in the case of S-type density in *Stage 2*.

6.4. The elongation of gravitational aggregates

The distribution of elongation values obtained in all numerical simulations are shown in Fig. 8. A sort of bimodal distribution can be seen corresponding to two main morphological families found: rounded and elongated aggregates. No correlation has been found between the aggregates elongation and their corresponding f_{LC} values nor their NAM. This seems to be a characteristic of the stochastic nature of the reaccumulation process that shows up in our simulations.

6.5. The porosity of gravitational aggregates

We generally find the porosities of the reaccumulated bodies are greater than 20%, as can be seen in Tables 1, 2 and 3. There are no significant differences between S and C-type asteroids; in fact, mean values are $33 \pm 5\%$ for S-type and $31 \pm 6\%$ for C-type. Fig. 9 shows the histogram of the values obtained for porosity for both S and C-type generated aggregates, including both *Stage 1* and *2* simulations.

Fig. 10 shows the distribution obtained for porosity as a function of f_{LC} (*Stage 1* and *2* simulations) for S and C-type asteroids. This result suggests that—although the distribution looks somewhat scattered—a clear trend may be identified for porosity to increase as the values of the mass fraction f_{LC} decrease. No remarkable difference shows up when discriminating different components density (S vs. C-type asteroids). It is interesting to point out that f_{LC} values larger than 0.30 imply porosity below 38%.

The outcome of asteroid impacts may go well beyond the conditions scaled from our laboratory impacts. In particular, for very energetic impacts, the amount of specific energy may be large and both f_{LF} and f_{LC} values would be smaller than those measured in such experiments. In order to expand the range of f_{LC} beyond the smallest values found in our *Stage 1* and *Stage 2* simulations, we have calculated the bulk volume and porosity of our simulated aggregates when we exclude the largest component. This artificial operation confirms the trend above, however, this extension of the porosity distribution has to be taken with care as it was not directly obtained by performing further numerical simulations. Due to the demanding CPU time, for operational reasons actual simulations in the $f_{LC} < 0.2$ range will be carried on in future work.

Fitting the porosity distribution corresponding to S- and C-types (only actual simulations) by a least-squares method gives:

S-type:

$$p_S = -0.318\ f_{LC} + 0.444 \tag{6}$$

C-type:

$$p_C = -0.515\ f_{LC} + 0.483 \tag{7}$$

For the joint distribution, we get:

$$p_{SC} = -0.425\ f_{LC} + 0.455 \tag{8}$$

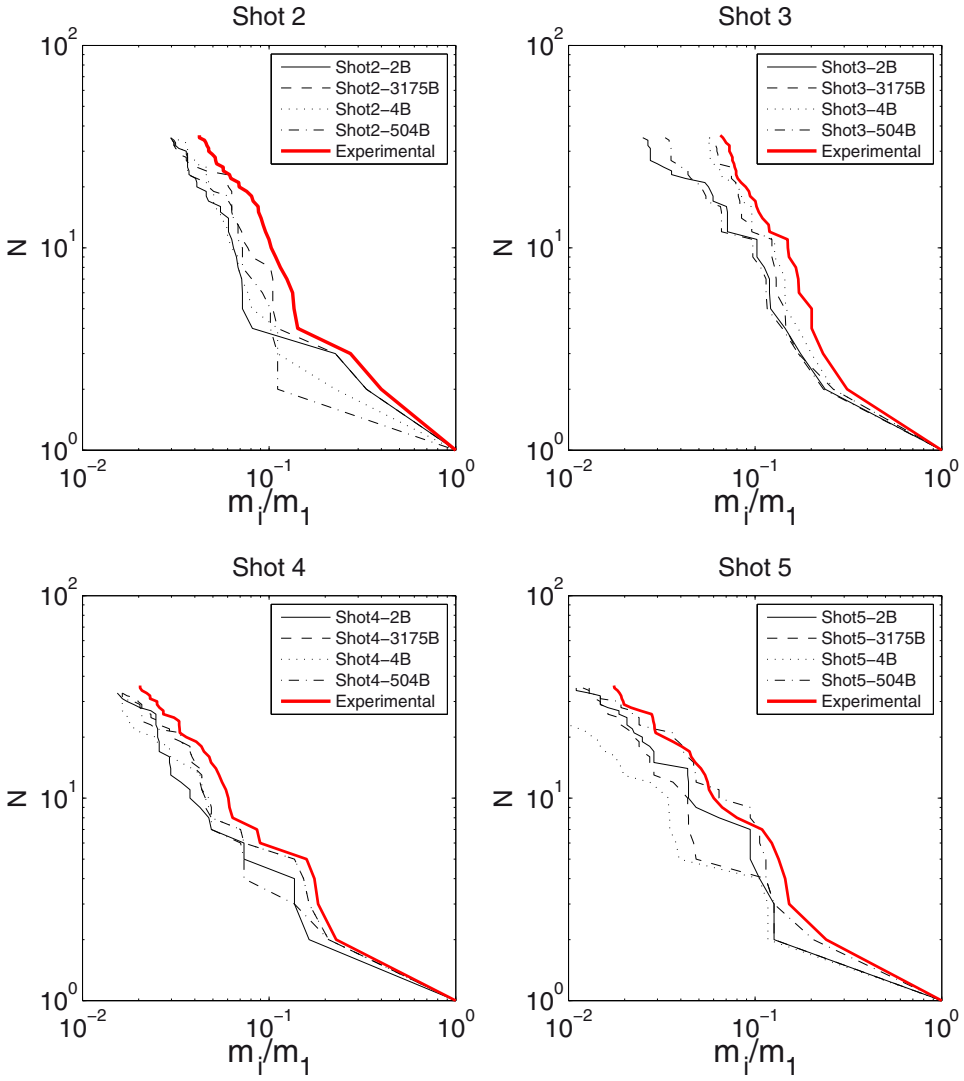

Fig. 5. Same as in Fig. 3 but in the case of C-type density in *Stage 2*.

The linear-correlation coefficient for these distributions are $r_S = 0.446$, $r_C = 0.556$ and $r_{SC} = 0.488$, which suggest a moderate correlation, as evident in the plot. Those relationships may be inverted to estimate the mass fraction of the largest component to the whole mass in any given structure for which an estimate of porosity is available.

No apparent correlation seems to exist between porosity and normalized angular momentum (NAM), let alone that there may be a loose trend for minimum porosity to grow at increasing values of normalized angular momentum.

6.6. Checking validity of results

6.6.1. Size range

Even if the nominal size of our synthetic aggregates is around 2 km, we wished to check if the obtained results are sensitive to a change of scale within the range of what can be classified as *small asteroids*. For this reason we varied the boundary conditions and the mass and size of the initial distribution of components to obtain different sizes of the reaccumulated objects. Two sets of simulations were performed to get aggregates of around 500 m and 10 km equivalent diameter, respectively. We chose 8 cases from the *Stage 2* set of simulations with different values of f_{LC} and different initial volume, so to inspect a wide range of initial mass distributions and f_{LC} values. The density of components was kept constant and we simply suitably scaled—in each case—the mass distribution and boundary volume. Initial velocity vectors and rotation spins of components were maintained constant so that angular momentum magnitude is scaled accordingly but the vector direction is not changed with respect to the nominal case.

Table 4 compiles the values of porosity, rotation period and elongation obtained by that further set of numerical simulations as compared to the nominal case. The comparison shows no significant difference in the porosity outcome. Elongation shows minor changes in many cases, as the shape of aggregates may be slightly different when the same situation is scaled in size.

Spin periods show changes up to a factor of 5, which means that scaling such systems in size (and mass) results in different rotation states corresponding to the same—but scaled in size—boundary conditions. However, the spin period distributions corresponding to each size scale are statistically indistinguishable, confirming the stochasticity of the large sequence of low-speed collisions that takes place before stabilization of the end structure is achieved.

6.6.2. Dependence on normal restitution coefficient.

As previously mentioned in Section 5.2, the effect of the normal restitution coefficient on simulation results is a delicate issue

Table 2
Simulations for *Stage 2* (S-type simulated aggregate asteroids), where numbers from 2.000 to 5.045 label the initial radius (R_0, in units of the radius R_e of the equivalent sphere whose mass is equivalent to the total mass of the components, as described in Section 5.3) of the volume within which the initial components are spatially distributed for each shot. Case A and B differ in the initial angular momentum of the whole structure. Symbols as in Table 1.

Shot	R_0	2.000		3.175		4.000		5.045	
		Case A	Case B	Case A	Case B	Case A	Case B	Case A	Case B
	f_{LC}	0.2834	0.2640	0.2848	N.R.	0.3083	N.R.	0.3111	N.R.
	NAM	0.0347	0.2933	0.1386	N.R.	0.3126	N.R.	0.1602	N.R.
Shot2	ρ	2491	2491	2405	N.R.	2290	N.R.	2509	N.R.
	P	0.3098	0.3101	0.3338	N.R.	0.3654	N.R.	0.3046	N.R.
	T	19.88	2.871	7.106	N.R.	3.951	N.R.	5.889	N.R.
	E	0.4098	0.4103	1.2652	N.R.	0.9198	N.R.	0.9638	N.R.
	f_{LC}	0.2117	0.2179	0.1998	0.1344	0.2107	N.R.	0.2300	N.R.
	NAM	0.0054	0.2543	0.0075	0.2508	0.0055	N.R.	0.0177	N.R.
Shot3	ρ	2403	2346	2386	2319	2180	N.R.	2344	N.R.
	P	0.3300	0.3457	0.3350	0.3562	0.3922	N.R.	0.3456	N.R.
	T	114.9	3.798	79.74	2.961	15.21	N.R.	37.10	N.R.
	E	0.2264	0.1768	0.0718	0.3183	1.1132	N.R.	0.3665	N.R.
	f_{LC}	0.3573	0.3945	0.3722	0.3730	N.R.	0.5575	0.4032	0.4286
	NAM	0.0410	0.1037	0.0518	0.2959	N.R.	0.1759	0.1158	0.0957
Shot4	ρ	2765	2726	2681	2308	N.R.	2589	2456	2606
	P	0.2249	0.2346	0.2479	0.3525	N.R.	0.2669	0.3099	0.2699
	T	12.41	5.545	10.98	3.156	N.R.	4.767	7.526	8.465
	E	0.2732	0.2839	0.4415	0.9462	N.R.	1.1114	0.8763	0.8936
	f_{LC}	0.4726	0.4256	0.4285	0.4439	0.3600	0.3615	0.3780	0.2030
	NAM	0.161	0.2192	0.2054	0.2040	0.1348	0.1739	0.4812	0.2109
Shot5	ρ	2731	2757	2649	2649	2481	2380	2559	2251
	P	0.2247	0.2199	0.2501	0.2439	0.3010	0.3293	0.2780	0.3722
	T	35.99	2.930	3.626	3.626	5.533	4.774	24.91	3.398
	E	0.3886	0.3744	0.4674	0.4666	0.6945	0.9008	1.0554	1.1811

Table 3
Same as Table 2 in the case of C-type simulated aggregate asteroids.

Shot	$R_0(R_{eq})$	2.000		3.175		4.000		5.045	
		Case A	Case B	Case A	Case B	Case A	Case B	Case A	Case B
	f_{LC}	0.3204	0.3504	0.2865	N.R.	0.3566	N.R.	N.R.	N.R.
	NAM	0.1653	0.7830	0.2132	N.R.	0.7986	N.R.	N.R.	N.R.
Shot2	ρ	1800	1815	1628	N.R.	1520	N.R.	N.R.	N.R.
	P	0.2515	0.2400	0.3236	N.R.	0.3674	N.R.	N.R.	N.R.
	T	6.2200	3.950	5.650	N.R.	63.30	N.R.	N.R.	N.R.
	E	0.4700	0.2110	0.8174	N.R.	1.2924	N.R.	N.R.	N.R.
	f_{LC}	0.1766	0.2290	0.2358	0.2590	0.2183	0.2341	0.2212	0.2383
	NAM	0.0846	0.3183	0.0567	0.3404	0.2069	0.3713	0.1062	0.5183
Shot3	ρ	1617	1545	1591	1403	1414	1477	1537	1482
	P	0.3253	0.3530	0.3336	0.4114	0.4086	0.3813	0.3570	0.3791
	T	12.72	5.130	19.04	5.131	6.620	6.640	12.52	4.800
	E	0.1995	0.2573	0.3412	0.3185	0.8806	0.3196	1.0699	0.1337
	f_{LC}	0.4236	0.4916	0.3764	0.4122	0.3979	N.R.	0.4048	0.4570
	NAM	0.1811	0.1466	0.0578	0.5895	0.2246	N.R.	0.0944	0.1982
Shot4	ρ	1795	1923	1787	1640	1512	N.R.	1768	1767
	P	0.2430	0.1864	0.2487	0.3089	0.3633	N.R.	0.2552	0.2534
	T	5.970	3.530	20.48	5.640	6.500	N.R.	11.73	4.790
	E	0.6002	0.3783	0.1906	0.3087	0.8541	N.R.	0.4784	0.8811
	f_{LC}	0.4185	0.4242	0.4625	N.R.	N.R.	0.3474	0.3629	N.R.
	NAM	0.1049	0.2450	0.3235	N.R.	N.R.	0.2099	0.1112	N.R.
Shot5	ρ	1779	1740	1813	N.R.	N.R.	1537	1574	N.R.
	P	0.2451	0.2616	0.2285	N.R.	N.R.	0.3508	0.3348	N.R.
	T	9.330	5.170	7.858	N.R.	N.R.	11.87	145.0	N.R.
	E	0.3125	0.3125	0.7043	N.R.	N.R.	1.2701	1.3205	N.R.

that needs to be checked to understand its potential implication on the interpretation of results. The nominal value is $\epsilon_N = 0.3$, which corresponds to rough surfaces and to measured values for rocks[1], as expected for asteroid components. $\epsilon_N = 0.5$ and 0.8 are two alternative values chosen to check the effect of this parameter. The latter value is typical of smooth glass, metallic and granite spheres. This check was performed by running 8 simulations for the nominal case corresponding to S-type meteorite analogue density. After checking the effect on the results, we extended the test to 4 cases corresponding to C-type components. Similarly to Section 6.6.1, we re-used the boundary and initial conditions of a subset of the simulations performed in *Stage 2*. In this case, every physical parameter and boundary condition is exactly the same, except for the ϵ_N value. The results of this final stage of simulations are gathered in Tables 5 and 6.

The most important conclusion that can be derived from this test is that the results obtained for porosity are very robust against

[1] https://www.rocscience.com/help/rocfall/webhelp/baggage/rn_rt_table.htm.

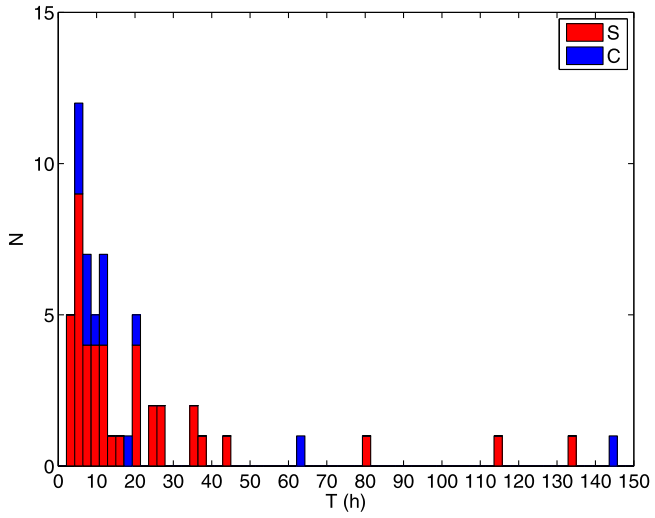

Fig. 6. Histogram of the spin period values for all simulations (except CASE B in *Stage 2*).

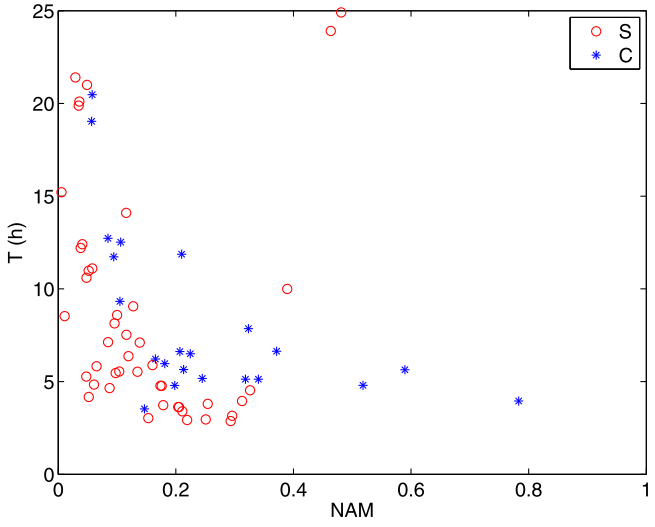

Fig. 7. Spin period as a function of NAM for S- and C-type generated aggregates for simulations in *Stage 1* and *Stage 2* (except CASE B).

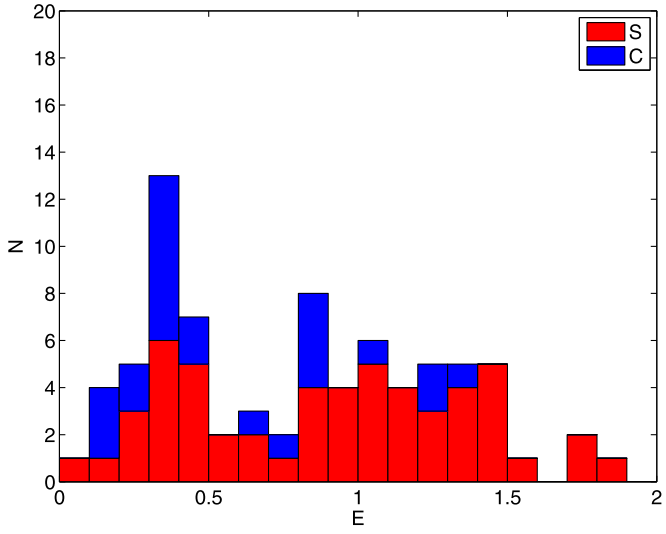

Fig. 8. Histogram of the values obtained for elongation—as defined in the text—corresponding to all the simulations run in *Stage 1* and *Stage 2*.

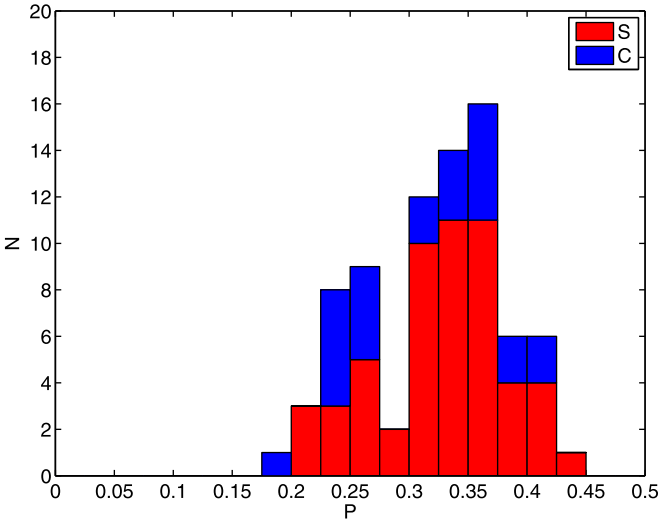

Fig. 9. Histogram of the values obtained for porosity for both S and C-type generated aggregate asteroids (*Stage 1* and *2* simulations).

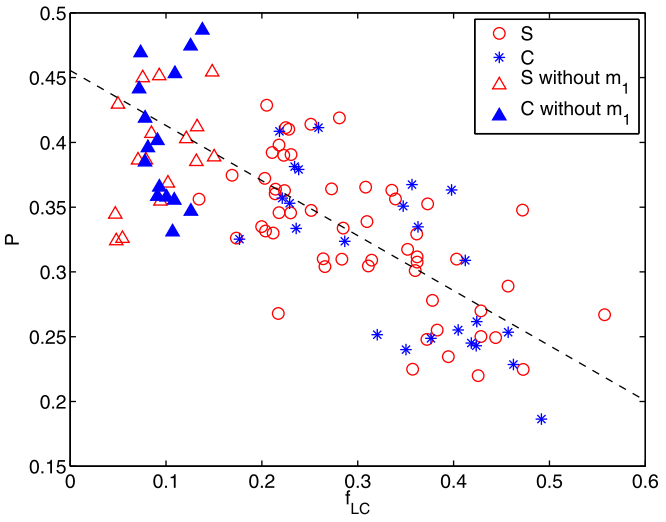

Fig. 10. Porosity as a function of f_{LC} for S and C-type generated aggregates (*Stage 1* and *2*). Triangles stand for porosity values obtained withdrawing the largest component from the simulated aggregates, as explained in the text (Section 7.2). Therefore, data points corresponding to $f_{LC} < 0.2$ have to be considered with care. An inverse linear trend for porosity as a function of f_{LC} is indicated by the broken line.

changes in ϵ_N, especially in the range of reasonable values for this parameter (0.3–0.5). This holds even for 2/3 of the test simulations run with $\epsilon_N = 0.8$; some instead (1/4) ended up with the system not completely aggregated. That is due to less efficient energy dissipation that may lead some of the components with relatively large kinetic energy to spend a large amount of time far from the rest of components before finally reaccumulate. However, values higher than 0.5 are probably not representative of real irregular shaped and rough rocky material, if they behave at asteroid scales as they do at typical terrestrial rock scale.

As for the results for elongation and spin period, the comparison for different values of ϵ_N shows again the stochastic nature of reaccumulation and differences in the final results clearly appear. Changing ϵ_N changes the outcome at any single rebound in unpredictable ways, generating different final shapes and therefore different spin periods.

Table 4
Comparison of results for S-type simulated aggregate asteroids, varying the size of the final aggregates (columns 2 to 4). Columns 5 to 7 indicate the boundary conditions under which the comparison is made.

	Final Size (km)			Boundary conditions		
	0.5 km	2 km	10 km	f_{LC}	R_0	Shot
	0.3272	0.3300	0.3345	0.2179	2.000	3
	0.2235	0.2249	0.2231	0.3945	2.000	4
	0.3471	0.3380	0.3325	0.2848	3.175	2
P	0.2549	0.2501	0.2189	0.4285	3.175	5
	0.3817	0.3654	0.3484	0.3120	4.000	2
	0.2892	0.3010	0.2812	0.3600	4.000	5
	0.3526	0.3456	0.3020	0.2300	5.045	3
	0.2785	0.3099	0.2610	0.4230	5.045	4
	49.23	114.9	80.32	0.2179	2.000	3
	12.41	5.545	19.31	0.3945	2.000	4
	4.083	7.106	3.711	0.2848	3.175	2
T (h)	3.346	3.626	11.66	0.4285	3.175	5
	8.771	3.951	12.07	0.3120	4.000	2
	12.02	5.533	7.173	0.3600	4.000	5
	50.51	37.10	71.41	0.2300	5.045	3
	38.50	7.526	6.475	0.4230	5.045	4
	0.1105	0.2264	0.1702	0.2179	2.000	3
	0.2732	0.2839	0.3646	0.3945	2.000	4
	1.3264	1.2652	1.2572	0.2848	3.175	2
E	0.7251	0.4674	0.5430	0.4285	3.175	5
	1.4626	0.9198	0.7137	0.3120	4.000	2
	0.7542	0.8023	0.7686	0.3600	4.000	5
	0.6748	0.3665	0.2686	0.2300	5.045	3
	2.3231	0.8763	0.8829	0.4230	5.045	4

Table 5
Comparison of results for S-type simulated aggregate asteroids, varying the value of the normal restitution coefficient. Columns 5 to 7 indicate the boundary conditions under which the comparison is made.

	ϵ_N(S)			Boundary conditions		
	0.3	0.5	0.8	f_{LC}	R_0	Shot
	0.3300	0.3299	0.3311	0.2117	2.000	3
	0.2249	0.1893	0.2488	0.3573	2.000	4
	0.3380	0.3492	N.R.	0.2848	3.175	2
P	0.2501	0.2575	0.2607	0.4228	3.175	5
	0.3654	0.3367	N.R.	0.3083	4.000	2
	0.3010	0.3046	0.3034	0.3600	4.000	5
	0.3456	0.3269	0.3190	0.2300	5.045	3
	0.3099	0.2679	N.R.	0.2300	5.045	4
	114.9	18.24	278.5	0.2117	2.000	3
	12.41	3.230	N.R.	0.3573	2.000	4
	7.106	9.841	5.045	0.2848	3.175	2
T (h)	3.626	4.546	4.330	0.4228	3.175	5
	3.951	95.89	N.R.	0.3083	4.000	2
	5.533	4.522	13.31	0.3600	4.000	5
	37.10	43.92	28.70	0.2300	5.045	3
	7.526	30.76	N.R.	0.2300	5.045	3
	0.2264	0.1370	0.1321	0.2117	2.000	3
	0.2732	0.4738	N.R.	0.3573	2.000	4
	1.2652	1.2633	1.5363	0.2848	3.175	2
E	0.4674	0.8416	0.8337	0.4228	3.175	5
	0.9198	1.7691	N.R.	0.3083	4.000	2
	0.6945	1.0384	0.1095	0.3600	4.000	5
	0.3665	0.4096	0.0960	0.2300	5.045	3
	0.8763	0.8747	N.R.	0.2300	5.045	4

7. Comparison with observable data

In this section we will try and compare the results of the numerical simulations carried out in this research with current observables to assess the validity of the study itself.

Table 6
Same as Table 5 in the case of C-type simulated aggregate asteroids. Columns 5 to 7 indicate the boundary conditions under which the comparison is made.

	ϵ_N(C)			Boundary conditions		
	0.3	0.5	0.8	f_{LC}	R_0	Shot
	0.2451	0.2525	0.2105	0.4211	2.000	5
P	0.3236	0.3398	0.3253	0.2865	3.175	2
	0.2487	0.2537	0.2774	0.3793	3.175	4
	0.4086	0.2822	0.2923	0.2183	4.000	3
	9.330	8.548	7.646	0.4211	2.000	5
T (h)	5.650	6.638	7.729	0.2865	3.175	2
	20.48	9.104	10.06	0.3793	3.175	4
	6.620	11.53	12.72	0.2183	4.000	3
	0.3125	0.8866	0.3820	0.4211	2.000	5
E	0.8174	0.4403	0.8172	0.2865	3.175	2
	0.1906	0.8167	0.3814	0.3793	3.175	4
	0.8866	0.1906	0.8867	0.2183	4.000	3

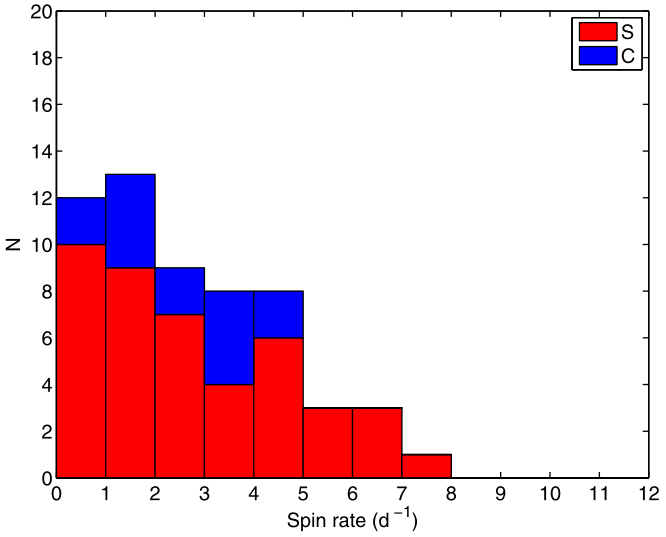

Fig. 11. Histogram of the normalized spin frequency of generated aggregates by numerical simulations, for both S and C-type asteroids.

7.1. Gravitational aggregates spins

The overall distribution of spin periods discussed in the following lines takes into account only those simulations for which the angular momentum of the system is a random variable at the beginning of simulations. That is, we explicitly exclude CASE B (in *Stage 2*). It has to be said that the angular momentum distribution resulting from the set up of our initial conditions is not a uniform distribution, as can be seen in Fig. 7. This shall likely affect the periods obtained for our GAs somewhat favoring long period outcomes. The median value for such synthetic distribution is 10.6 h. This value can be compared with the observational median value by Donnison (2003) (8.5 h). The difference in the median may be affected by the absence of fast rotators ($T < 3$ h) in our sample when angular momentum is random (no CASE B).

We obtain 21% (12 over 57 synthetic aggregates) slow rotators ($T > 24$ h). The obtained ratio is in agreement with observational measurements by Pravec et al. (2008) (21%: 56/268 asteroids in the 3–15 km range).

The distribution of the simulation results for spin frequency shown in Fig. 11 can be compared with the spin frequency distribution in Pravec et al. (2008). On one hand the distribution is similar to the one shown by these authors, in particular in the excess of slow rotators. The fact that objects with very long rotation periods naturally appear in the process of re-accumulation

could help in the search for the origin and explanation of what are known as slow rotators. On the other hand our synthetic distribution shows a lack of fast rotators as compared to those authors. It is hard to compare the distribution of fast rotators in our synthetic sample with that from observables. In fact, YORP effect at the size range of validity of our simulations is heavily affecting currently observed populations. YORP is more efficient as the distance to the Sun decreases, which is the case of NEAs for which fast spin periods have been measured. Considering an overall spin distribution, we may define fast rotators as those with a period smaller than half the average value of the distribution, in this case we get 14% such objects, half the percentage that can be derived from Pravec et al. (2008). On one hand, this discrepancy may be explained by the fact that after their formation as aggregates, asteroids undergo a variety of phenomena potentially increasing their spin rate, such as collisions, and especially YORP effect. On the other hand, YORP has been invoked to explain some of the slow rotators as well, at least in the case of NEAs.

For the same reasons, minimum values for spin periods of simulated aggregates do not match observed ones. The minimum value for the rotation period of the simulated S-type bodies is 2.9 h, when including simulation runs with increased angular momentum, while observations give the well-known 2.2 h limit as a minimum period (Pravec and Harris, 2000). In the case of simulations for C-type objects, the minimum value is 3.5 h, while the fastest carbonaceous asteroids have periods around 3.0 h. However, matching the fast spin end of the asteroids distribution was not the goal of this work, in order to do that, we should have tried increasing values of initial angular momentum. A dedicated study of the spin up evolution of aggregates and how that affects binary systems and pairs production is planned to be the next step of our investigation.

Further caution has to be made as comparisons are made with observational populations whose members are likely mostly, but not necessarily all, gravitational aggregates.

In conclusion, little can really be said about the consistency of the comparison between our results for spin periods and measured periods for real asteroids. We just would like to introduce the idea that gravitational accumulation may play a role in the explanation of the existence of slow rotators.

7.2. Gravitational aggregates porosity

Carry (2012) compiled a detailed list of density measurements of all asteroid types and estimated values for their porosities. He included a reference accuracy for the measured or estimated values provided in the list. We use this work as a baseline to check the validity of our results and we complement those data with recent accurate measurements of asteroid density and porosity. In order to have a reliable sample with which to compare our results for porosity, we only take into account asteroids in Carry's list and recent observations whose density estimation has at least a 20% accuracy. Also, to avoid including monolithic asteroids in that sample, we take into account objects with estimates of porosity larger than 10% and belonging only to S- and C-type asteroids.

With these conservative requirements we end up with a sample of 9 S-type and 25 C-type asteroids. The corresponding average values of porosity are 0.28 ± 0.14 and 0.42 ± 0.18, respectively. These data are quite dispersed around the mean values but may be used as reference values to check our results.

In our numerical simulations, for all S- and C-type objects in *Stage 1* and *Stage 2*, we obtained a mean porosity of 0.33 ± 0.05 (S-type) and 0.31 ± 0.06 (C-type). No significant difference was found between these two classes. Recall that the only difference between our synthetic S- and C-types is the density of components. Therefore, it can be stated that according to our numerical simulations a change in density within a reasonable range of values does not significantly alter the average dynamical and collisional process of reaccumulation of the components from any initial random distribution that leads to the formation of a gravitational aggregate asteroid.

The mean porosity obtained from the numerical simulations in the case of S-type asteroid aggregates is reasonably close to the estimated mean value from observational data, which is an encouraging test of the validity of our results. From that comparison, and from the results obtained in Section 6.5, we may conclude that the largest component of most of the S-type aggregate asteroids may have a mass larger than $15 - 20\%$ of the mass of the whole body.

The analysis of the results for the case of C-type asteroids is especially interesting. In this case, even if numerical simulations and observable estimates agree within error estimates, it is evident that there is large discrepancy between mean values (0.31 vs. 0.42). Comparing the two sets of means using a Student's *t*-test, the probability that the two C-type means represent the same distribution is 6.25 times smaller than in the case of the comparison for the two S-type means. Therefore it is reasonable to say that the simulated and observable C-type porosity distributions are significantly different. However, if we focus on porosity values in our simulation results for C-type corresponding to the estimated values for $f_{LC} < 0.15$ or to the linear relationship found in Section 6.5, it is easy to show that we get a porosity value of 0.40 ± 0.05, quite in the range of estimated C-type asteroids porosity.

Based on these considerations we suggest that most of the C-type reaccumulated asteroids may have an internal structure such that their major component should be a fraction not larger than 15% of the total mass. This would be a significant difference in the internal structure of C- with respect to S-type aggregates.

The reason of this difference in internal structure could be the higher fragility of C-type (mostly carbonaceous) asteroids in collisions compared to the S-type (mostly silicate) asteroids (Scheeresm et al., 2015, e.g.). This can be expressed in terms of their resistence to shattering (impact strength) or its related magnitude: the threshold specific energy for fragmentation (Q_S^*). It was shown in catastrophic collision laboratory experiments carried out in the last decades, that the threshold specific energy for fragmentation in fragile materials is lower than that of stronger materials. This implies that objects of equal mass but with different resistence to collisions (for instance, S and C types) will suffer different structural damage under the same impact kinetic energy E_k. As noted in Section 3, f_{LF} depends on Q_S^*/E_k, therefore, materials with low Q_S^*—as in the case of C-type asteroids—will produce smaller f_{LF} than in the case of high Q_S^* values, and that will affect the value of f_{LC} in the corresponding aggregate structure.

However, alternative explanations for the difference in observed S- and C-type porosity cannot be ruled out:

I. Volumes of asteroids may be often overestimated in the case of C-type asteroids. One (not the only) source of error is the determination of their geometric albedo (p_v) that affect size estimates. C-types typically have values lower than S-type asteroids' and are difficult to determine. The estimated size is mostly derived from albedo, $D \propto \sqrt{p_v}$; many low albedo values might be overestimated so that objects whose volume is deduced by size determined with this method could critically contribute to raise the average value of the estimated porosities of C-type asteroids.

II. An interesting alternative explanation for high C-type porosity values could be that the components of C-type aggregate asteroids are intrinsically more porous than their meteoritic analogues. That is to say, the components that form these aggregates (tens to hundreds of meters of size) may have more void space in their interior in the form of cracks or other gaps at meter-size scales than their meteorite analogues of a few cm (or tens of cm, as in the unique case of the largest fragment of the Allende mete-

orite). Those hypothetical structural voids would end up reducing the overall body density and increasing porosity estimations to observed values. Beyond the intrinsic fragility of carbonaceous chondrites, the mentioned possible structural porosity may also contribute to help and explain the fact that, although the probability of falling for meteorites corresponding to both (S and C) classes is similar, the abundance of carbonaceous chondrites is an order of magnitude lower than that of ordinary chondrites. This difference in the survival against atmosphere crossing may come from the very structure of C-type asteroids, which may be intrinsically more porous than the samples recovered on Earth. Thus, macro-porosity estimates of C-type asteroids, based on the measured porosity of their meteoritic analogues, might be overestimated due to the material intrisic structural diversity.

8. Conclusions

We have performed 144 total numerical simulations using *pkdgrav* code to explore the self-gravity reaccumulation behaviour of monolithic bodies randomly dispersed in limited space volumes with mass frequency distributions extracted from laboratory collisional experiments. 118 of those simulations resulted in gravitational aggregates. The analysis of the results of such simulations lead to the following conclusions.

- Our results do not show significant difference in average values of porosity, spin period and elongation, when changing the density of components within the typical range of carbonacous chondrites to ordinary chondrites meteorite analogues (2500 to 3500 kg/m^3). This implies that changes in density in this range do not significantly alter the dynamical and collisional processes that determine the reaccumulation of the components from given boundary conditions. We also find scale independence of the results for the evolution of the reaccumulation of systems which differ in mass up to four orders of magnitude (about a factor of 20 in size).
- No correlation was found for porosity, spin period and elongation as a function of angular momentum nor initial volume boundary conditions of the components distribution. Also spin period and elongation do not show any dependence on the largest component mass ratio. This reflects the fact that the reaccumulation process is very stochastic, for which the effects of random sequences and outcomes of small-speed collisions between components overcome most effects on the process due to boundary conditions.
- The average value of the calculated macroporosity of the final aggregates of our numerical simulations matches the average porosity of S-type asteroids known with a precision better than 20%. This implies that the internal structure of S-type asteroids is compatible with largest component mass ratios in the $0.15 < f_{LC} < 0.5$ range.
- Porosities of C-type asteroids estimated at the same precision level as S-type asteroids are not matched by the average value of the porosities calculated for our simulated aggregates in the same range of largest fragment mass ratios as S-type asteroids. Instead, the match is very close when considering mass ratios below 15%. We give three possible interpretations to this result: (1) It may well be that C-type asteroids predominantly have smaller largest component mass fractions with respect to S-type asteroids as a consequence of their larger fragility in the face of the corresponding critical specific energy for fragmentation (Q_S^*). (2) Volumes may be systematically overestimated for C-type asteroids due to overestimation of their albedo values. (3) It may be the case that most carbonaceous chondrites (the meteorite analogues of C-types) are not fully representative of their parent bodies. In fact, the few samples available on Earth are tens of cm in size and may have been embedded in large (tens of meters) more porous coherent structures. Such structures would then have larger bulk porosities than those remnant meteorites and they would be the components of C-type gravitational aggregates. The difference between the $\sim$30% porosity found by numerical simulations and the $\sim$40% values measured for C-types would therefore be due to up to $\sim$10% higher intrinsic bulk porosity of the aggregate components of such asteroids.
- We find an inverse linear trend relationship for porosity as a function of mass fraction f_{LC}, for both S-type and C-type objects. This circumstance may be used to infer information about asteroid interior structure of asteroids with reliable spectral composition and accurate bulk porosity estimations such as those visited by space probes. In particular, inferred values of f_{LC} may be taken as seeds to generate suitable mass-frequency distributions to match the measured mass of a given aggregate asteroid.
- Simulations have been checked against different values of the normal restitution coefficient for low-speed collisions between components in the reaccumulation phase. Changes in this parameter do not affect the porosity values of the obtained aggregates. However, it randomly influences their rotational periods and overall shape. This is particularly true for high values of the restitution coefficient and is related to the stochasticity introduced in the small-speed collisions between components, which are responsible for final aggregate configurations.

Acknowledgements

This work has been possible thanks to the grants AYA2008-06202C0303 and AYA2011-30106-C02-02 by the extinct Spanish Ministerio de Ciencia e Innovación.

References

Abe, M., Takagi, Y., Kitazato, K., Abe, S., Hiroi, T., Vilas, F., Clark, B.E., Abell, P.A., Lederer, S.M., Jarvis, K.S., Nimura, T., Ueda, Y., Fujiwara, A., 2006. Near-infrared spectral results of asteroid Itokawa from the Hayabusa spacecraft. Science 312 (5778), 1334–1338.

Asphaug, E., 1999. Survival of the weakest. Nature 402 (6758), 127–128.

Ballouz, R.-L., Richardson, D.C., Michel, P., Schwartz, S.R., 2014. Rotation-dependent catastrophic disruption of gravitational aggregates. Astrophys. J. 789, 158.

Ballouz, R.-L., Richardson, D.C., Michel, P., Schwartz, S.R., Yu, Y., 2015. Numerical simulations of collisional disruption of rotating gravitational aggregates: dependence on material properties, 107, pp. 29–35.

Benavidez, P.G., Durda, D.D., Enke, B., Campo Bagatin, A., Richardson, D.C., Asphaug, E., Bottke, W.F., 2017. Impact simulation in the gravity regime: exploring the effects of parent body size and internal structure. Icarus in press doi:10.1016/j.icarus.2017.05.030.

Benavidez, P.G., Durda, D.D., Enke, B.L., Bottke, W.F., Nesvorný, D., Richardson, D.C., Asphaug, E., Merline, W.J., 2012. A comparison between rubble-pile and monolithic targets in impact simulations: application to asteroid satellites and family size distributions. Icarus 219, 57–76.

Benz, W., Asphaug, E., 1999. Catastrophic disruptions revisited. Icarus 142, 5–20.

Bottke Jr., W.F., Richardson, D.C., Love, S.G., 1997. Can tidal disruption of asteroids make crater chains on the earth and moon? Icarus 126, 470–474.

Campo Bagatin, A., Petit, J.-M., 2001. Effects of the geometric constraints on the size distributions of debris in asteroidal fragmentation. Icarus 149, 210–221.

Campo Bagatin, .A., Petit, J.-M., Farinella, P., 2001. How many rubble piles are in the asteroid belt? Icarus 149, 198–209.

Carry, B., 2012. Density of asteroids. Planet. Space Sci. 73, 98–118.

Chapman, C.R., 1978. Asteroid collisions, craters, Regoliths, and lifetimes. In: Morrison, D., Wells, W.C. (Eds.), Asteroids: An Exploration Assessment, pp. 145–160.

Chapman, C.R., 2002. Cratering on asteroids from galileo and NEAR schoemaker. In: Bottke, W., Cellino, A., Paolicchi, P., Binzel, R. (Eds.), Asteroids III. University of Arizona Press, Tucson, pp. 315–330.

Cheng, A.F., 2002. Near-Earth asteroid rendezvous: mission summary. In: Bottke, W., Cellino, A., Paolicchi, P., Binzel, R. (Eds.), Asteroids III. Univesity of Arizona Press, Tucson, pp. 351–366.

Cheng, A.F., 2004. Implications of the NEAR mission for internal structure of Mathilde and Eros. Adv. Space Res. 33, 1558–1563.

Chesley, S.R., Farnocchia, D., Nolan, M.C., et al., 2014. Orbit and bulk density of the OSIRIS-REx target asteroid (101955) bennu. Icarus 235, 5–22.

Cundall, P.A., Strack, O.D.L., 1979. A discrete numerical model for granular assemblies. Geotechnique 29 (1), 4765.

Donnison, J.R., 2003. Statistical evidence for fast and slow asteroid rotations using Bayesian methods. MNRAS 338, 452–456.

Durda, D.D., Bottke, W.F., Enke, B., Merline, W.J., Asphaug, E., Richardson, D.C., Leinhardt, Z.M., 2004. The formation of asteroid satellites in large impacts: results from numerical simulations. Icarus 167, 382–396.

Durda, D.D., Bottke, W.F., Nesvorný, D., Enke, B.L., Merline, W.J., Asphaug, E., Richardson, D.C., 2007. Size-frequency distributions of fragments from SPH/n-body simulations of asteroid impacts: comparison with observed asteroid families. Icarus 186, 498–516.
Durda, D.D., Campo, B.A., Alemañ, R.A., Flynn, G.J., Strait, M.M., Clayton, A.N., Patmore, E.B., 2015. The shapes of fragments from catastrophic disruption events: effects of target shape and impact speed. Planet. Space Science 107, 77–83.
Durda, D.D., Richardson, D.C., Asphaug, E., Moshovitz, N., 2013. Size dependence of the coefficent of restitution: small scale experiments and the effects of rotation. In: Lunar and Planetary Science XLIV, LPI Houston, p. 2263.
Farinella, P., Paolicchi, P., Zappala, V., 1981. Collisional origin of the asteroid families: Mass and velocity distributions. Astron. Astrophys. 104, 159.
Fujiwara, A., Kamimoto, G., Tsukamoto, A., 1977. Destruction of basaltic bodies by high-velocity impact. Icarus 31, 277–288.
Giblin, I., 1998. New data on the velocity-mass relation in catastrophic disruption. Planet. Space Sci. 35 (7), 921–928.
Holsapple, K., Giblin, I., Housen, K., Nakamura, A., Ryan, E., 2002. Asteroid Impacts: Laboratory Experiments and Scaling Laws. In: Bottke, W.F, Cellino, A., Paolicchi, P., Binzel, R.P (Eds.). In: Asteroids III. University of Arizona Press, Tucson, pp. 443–462.
Holsapple, K.A., 2007. Spin limits of solar system bodies: from the small fast-rotators to 2003 EL61. Icarus 187, 500–509.
Jeffreys, H., 1947. The relation of cohesion to Roche's limit. Mon. Not R Astron Soc 107, 260–272.
Jutzi, M., Michel, P., Benz, W., Richardson, D.C., 2010. Fragment properties at the catastrophic disruption threshold: the effect of the parent bodys internal structure. Icarus 207, 54.
Korycansky, D.G., Asphaug, A., 2006. Low-speed impacts between rubble piles modeled as collections of polyhedra. Icarus 181, 605–617.
Leinhardt, Z.M., Richardson, D.C., Quinn, T., 2000. Direct n-body simulations of rubble pile collision. Icarus 146, 133–151.
Leinhardt, Z.M., Stewart, S.T., 2009. Full numerical simulations of catastrophic small body collisions. Icarus 199, 542–559.
Love, S.G., Ahrens, T.J., 1996. Catastrophic impacts on gravity dominated asteroids. Icarus 124 (1), 141–155.
Melosh, H.J., Ryan, E.V., 1997. NOTE: Asteroids: shattered but not dispersed. Icarus 129, 562.
Melosh, H.J., Schenk, P., 1993. Estimate of the size of comet shoemaker-levy 9 from a tidal breakup model. Nature 365, 733–735.
Michel, P., Benz, W., Richardson, D.C., 2004. Catastrophic disruption of asteroids and family formation: a review of numerical simulations including both fragmentation and gravitational reaccumulations. Planet. Space Sci. 52, 1109–1117.
Michel, P., Benz, W., Tanga, P., Richardson, D.C., 2001. Collisions and gravitational reaccumulation: forming asteroid families and satellites. Science 294, 1696–1700.
Michel, P., Richardson, D.C., 2013. Collision and gravitational reaccumulation: possible formation mechanism of the asteroid Itokawa. A& A 554, L1.
Michel, P., Richardson, D.C., Durda, D.D., Jutzi, M., Asphaug, E., 2015. Collisional Formation and Modeling of Asteroid Families. In: Michel, P., DeMeo, F.E, Bottke, W.F (Eds.), Asteroids IV. University of Arizona Press, Tucson, pp. 341–354.
Michel, P., Tanga, P., Benz, W., Richardson, D.C., 2002. Formation of asteroid families by catastrophic disruption: simulations with fragmentation and gravitational reaccumulation. Icarus 160, 10–23.
Miyamoto, H., Yano, H., Scheeres, D., Sasak, S., Barnouin-Jha, O.S., Gaskel, R.W., Cheng, A.F., Demura, H., Fujiwara, A., Hashimoto, T., Hirata, N., Hond, C., Ishiguro, M., Kubot, T., Michikami, T., Nakamura, A.M., Nakamura, R., Saito, J., Yokota, Y., Hayabusa, T., 2006. Regolith on a tiny asteroid: granular materials partly cover the surface of Itokawa. In: Proceedings of the 37th Annual Lunar and Planetary Science Conference League City, Texas, pp. 13–17. March, 2006, abstract 1686.
Nakamura, A., Fujiwara, A., 1991. Velocity distribution of fragments formed in a simulated collisional disruption. Icarus 92, 132–146.
Opik, E., 1950. Roche'S limit: rings of saturn. Irish Astron. J. 1, 25–26.
Petit, J.-M., Farinella, P., 1993. Modelling the outcomes of high-velocity impacts between small solar system bodies. Celestial Mech. Dyn. Astron. 57, 1–28.
Pravec, P., Harris, A.W., 2000. Fast and slow rotation of asteroids. Icarus 148, 12–20.
Pravec, P., Harris, A.W., Vokrouhlický, D., Warner, B.D., Kusnirak, P., Hornoch, K., Pray, D.P., Higgins, D., Oey, J., Galad, A., Gajdos, Korno, L., Vilagi, J., Husarik, M., Krugly, Y.N., Shevchenko, V., Chiorny, V., Gaftonyuk, N., Cooney Jr., W.R., Gross, J., Terrell, D., et al., 2008. Spin rate distribution of small asteroids. Icarus 197, 497–504.
Richardson, D.C., 1995. A self-consistent numerical treatment of fractal aggregated dynamics. Icarus 115, 320–335.
Richardson, D.C., Bottke, W.F., Love, S.G., 1998. Tidal distortion and disruption of Earth-crossing asteroids. Icarus 134, 47–76.
Richardson, D.C., Elankumaran, P., Sanderson, R.E., 2005. Numerical experiments with rubble piles: equilibrium shapes and spins. Icarus 173, 349–361.
Richardson, D.C., Leinhardt, Z.M., Bottke, J.W.F., Melosh, H.J., Asphaug, E., 2002. Gravitational aggregates: evidence and evolution. In: Bottke Jr., W.F., Cellino, A., Paolicchi, P., Binzel, R.P. (Eds.), Asteroids III. University of Arizona Press, Tucson.
Richardson, D.C., Michel, P., Walsh, K.J., Flynn, K.W., 2009. Numerical simulations of asteroids modelled as gravitational aggregates with cohesion. Planet. Space Sci. 57, 183–192.
Richardson, D.C., Quinn, T., Stadel, J., Lake, G., 2000. Direct large-scale n-body simulations of planetesimal dynamics. Icarus 143, 45–59.
Saito, J., Miyamot, H., Nakamura, R., Ishiguro, M., Michikami, T., Nakamura, A.M., Demur, H., Sasaki, S., Hirata, N., Honda, C., Yamamoto, A., Yokota, Y., Fus, T., Yoshid, F., Tholen, D.J., Gaskell, R.W., Hashimoto, T., Kubota, T., Higuchi, Y., Nakamura, T., Smith, P., Hiraoka, K., Honda, T., Kobayashi, S., Furuya, M., Matsumoto, N., Nemoto, E., Yukishita, A., Kitazato, K., Dermawan, B., Sogame, A., Terazono, J., Shinohara, C., Akiyama, H., 2006. Detailed images of asteroid 25143 Itokawa from Hayabusa. Science 312 (577), 1341–1344.
Sanchez, P., Scheeres, D.J., 2012. DEM Simulation of rotation-induced reshaping and disruption of rubble-pile asteroids. Icarus 218, 876–894.
Scheeresm, D.J., Britt, D., Carry, B., Holsapple, K.A., 2015. Asteroid interiors and morphology. In: Michel, P., DeMeo, F.E., Bottke, W.F. (Eds.), Asteroids IV. University of Arizona Press, Tucson, pp. 745–766.
Schwartz, S.R., Richardson, D.C., Michel, P., 2012. An implementation of the soft--sphere discrete element method in a high-performance parallel gravity tree–code. Granular Matter 14, 363–380.
Stadel, J.G., 2001. Cosmological N-body Simulations and Their Analysis. University of Washington Ph.D. thesis. Feb 2002, 141 pages
Takeda, T., Ohtsuki, K., 2007. Mass dispersal and angular momentum transfer during collisions between rubble-pile asteroids. Icarus 189, 256–273.
Takeda, T., Ohtsuki, K., 2009. Mass dispersal and angular momentum transfer during collisions between rubble-pile asteroids. II. Effects of initial rotation and spin–down through disruptive collisions. Icarus 202, 514.
Tanga, P., et al., 2009. Rubble-pile reshaping reproduces overall asteroid shapes. Astrophys. J. Lett. 706, 197–202.
Tanga, P., Cellino, A., Michel, P., Zappala, V., Paolicchi, P., Dell'Oro, A., 1999. On the size distribution of asteroid families: the role of geometry. Icarus 141, 65–78.
Thomas, P., Prockter, L., 2010. Tectonics of small bodies. in planetary tectonics. Cambridge University, Cambridge, pp. 234–264.
Walsh, K.J., Richardson, D.C, Michel, P., 2012. Spin-up of rubble-pile asteroids: disruption, satellite formation and equilibrium shapes. Icarus 220, 514–529.
Walsh, K.J., Richardson, D.C., Michel, P., 2008. Rotational breakup as the origin of small binary asteroids. Nature 454 (7201), 188–191.
Walsh, K.J., Richardson, D.C., 2006. Binary near-Earth asteroid formation: rubble pile model of tidal disruptions. Icarus 180, 201–216.
Yoshikawa, M., Kawaguchi, J., Fujiwara, A., Tsuchiyama, A., 2015. Hayabusa sample return mission. in asteroids IV. University of Arizona Press, Tucson, pp. 397–418.
Yu, Y., Richardson, D.C., Michel, P., Schwartz, S.R., Ballouz, R.-L., 2014. Numerical predictions of surface effects during the 2029 close approach of asteroid 99942 apophis. Icarus 242, 8296.